# Scale-dependent Air-Sea Mechanical Coupling: Resolution Mismatch and Spurious Eddy-Killing

**Shikhar Rai[1], Matthew Hecht[2], Mathew Maltrud[2], Hussein Aluie[1]**

[1]University of Rochester
[2]Los Alamos National Laboratory
[1]Rochester, NY 14627
[2]Los Alamos, NM 87545

**Key Points:**

- Disproportionate effect of small-scale winds of O(100) km on mesoscale ocean eddies
- Current bulk wind stress formulations suffer from significant biases at oceanic mesoscales
- A simple reformulation of wind stress corrects for the bias

Corresponding author: Shikhar Rai, `shikhar.rai@rochester.edu`

Corresponding author: Hussein Aluie, `hussein@rochester.edu`

## Abstract

Mechanical coupling of the atmosphere to the ocean surface in general circulation models is represented using bulk wind stress formulations. The stress is often based on either absolute wind velocity, $\boldsymbol{\tau}_a$, or the more correct wind velocity relative to the ocean surface currents, $\boldsymbol{\tau}_r$. Here, we use coarse-graining to disentangle wind work by these formulations at different length-scales. We show that both can be reasonably accurate in forcing the ocean at length-scales larger than the mesoscales, with $\boldsymbol{\tau}_a$ overestimating wind work by 10%. However, $\boldsymbol{\tau}_a$ and $\boldsymbol{\tau}_r$ show stark and opposing systematic biases in how they drive the mesoscales; $\boldsymbol{\tau}_a$ does negligible (albeit positive) work on the mesoscales, while $\boldsymbol{\tau}_r$ yields eddy-killing (negative work) that is artificially exaggerated by a factor of $\approx 4$. We derive an analytical criterion for eddy-killing to occur, which shows that exaggerated eddy killing is due to resolution mismatch between the atmosphere and ocean. Our criterion highlights the disproportionate effect small-scale winds $O(100)$ km can have on the dynamics of mesoscale ocean eddies, despite the dominant atmospheric motions being at length-scales larger than $O(10^3)$ km. The eddy-killing criterion shows that large-scale winds do not necessarily cause eddy-killing but are merely an amplification factor for wind work on the mesoscales, which can be either positive or negative depending on the local alignment of small-scale winds with the ocean eddies. We propose a simple reformulation of $\boldsymbol{\tau}_r$, without introducing tuning parameters, to remove spurious eddy-killing from air-sea resolution mismatch that is often present in climate models.



## Plain Language Summary

It is widely appreciated that winds are the primary driver of the general oceanic circulation. This is why any systematic biases in how the atmosphere couples to the ocean in climate models is of great interest. Here, we build upon a previous study (Rai et al., 2021) showing that wind provides energy to large length-scales ($>$ 260 km) and extracts energy from the smaller mesoscales at a rate of $\approx$ 50 GW by a process called "eddy-killing." We find that the manner with which air-sea coupling is represented in models can have significant impact on the evolution of mesoscale eddies. We identify mismatch in resolution between the atmosphere and ocean components of a model as leading to a systematic bias toward exaggerated eddy-killing in the ocean. Such resolution mismatch is ubiquitous in climate models, where the atmosphere is almost always of a coarser resolution than the ocean, preventing the oceanic mesoscales from coupling to the atmosphere. In this work, we propose a simple fix for the bias without requiring that the ocean and atmosphere be at the same resolution.


## 1 Introduction

Wind is the main driver of the general oceanic circulation (Wunsch et al., 2004). Although the net path of mechanical energy is from the atmosphere to the ocean, several recent studies have shown evidence that oceanic "mesoscale eddies"[1] actually lose energy to the atmosphere (e.g., Dewar & Flierl, 1987; Zhai & Greatbatch, 2007; Flexas et al., 2019; Rai et al., 2021), in a process sometimes called *eddy killing* (Renault, Molemaker, Gula, et al., 2016).

It is estimated that wind stress injects $\approx$ 4-5 TW into the quasi-steady[2] surface ocean flow (Flexas et al., 2019), of which $\approx$ 2.4 TW goes into surface Ekman flow (Wang & Huang, 2004a), and $\approx$ 0.5-0.7 TW into near-inertial oscillations (Watanabe & Hibiya, 2002; Alford,

[1] We put the word in quotes since the characterization and definition of mesoscale eddies has not been consistent among these studies, as we elaborate below.

[2] "Quasi-steady" refers to frequencies much lower than those of surface waves, into which the wind injects $\approx$ 60 TW (Wang & Huang, 2004b) and is mostly dissipated in the surface layer.

2003). Most of this power is dissipated within the Ekman layer limited to the upper tens of meters and, as a result, does not contribute directly to the general circulation (Wunsch, 1998). Of the wind-driven ocean circulation, it is wind work on the geostrophic flow that is passed to the deep ocean below the Ekman layer (Von Storch et al., 2007).

Earlier studies (Wunsch, 1998; Von Storch et al., 2007) estimated wind work into the geostrophic flow to be $\approx 1$ TW. These estimates relied on "absolute" wind stress, $\boldsymbol{\tau}_a$, based on wind velocity $\mathbf{u}_a$ alone. Duhaut and Straub (2006) argued that ignoring ocean surface current in surface wind stress formulation leads to an overestimation of wind work by 20%-35%. This was subsequently supported by studies with eddy resolving, fully coupled models (Dawe & Thompson, 2006; Zhai & Greatbatch, 2007; Eden & Dietze, 2009), and also from wind scatterometer observations by Hughes and Wilson (2008). They showed that global wind work decreases by 190 GW, down to 760 GW, when the physically correct wind velocity, $\mathbf{u}_r = \mathbf{u}_a - \mathbf{u}_o$ relative to that of the ocean surface $\mathbf{u}_o$, is used in the bulk stress formulation (Scott & Xu, 2009). It naturally follows that use of relative winds, which are generally of smaller magnitude than absolute winds especially in regions of strong wind-aligned ocean currents, will cause a reduction in wind work even in absence of eddies. This reduction of wind work is sometimes conflated with eddy killing. Indeed, our results below show that eddy killing contributes only partially (albeit $> 50\%$) to the reduction of wind work.

From a fundamental standpoint, understanding how wind drives the ocean is essential to understanding the oceanic general circulation (Wunsch, 1998). For example, it helps us determine the extent to which the large-scale ocean currents are driven directly (*i.e.* in a geographically local sense) by wind compared to other indirect mechanisms such as due to conversion from potential energy or global (*i.e.* geographically nonlocal) balances (Vallis, 2017). In this paper, we quantify the extent to which large-scale western boundary currents (WBCs), including the Gulf Stream and Kuroshio, are forced directly by wind. Analyzing wind work at different scales also helps in understanding the dissipation pathways for the mesoscales, which is a longstanding problem in physical oceanography (Ferrari & Wunsch, 2009). The mesoscales account for a majority of the ocean's kinetic energy (Storer et al., 2022) and are, therefore, a critical component of the global circulation (Stammer, 1997), playing a leading role in the transport of heat and biogeochemical tracers (e.g., Dufour et al., 2015; Mémery et al., 2005; Garçon et al., 2001). An accumulation of recent evidence indicates that wind forcing is an important energy sink for the mesoscales, especially in strongly eddying regions such as WBCs (C. Xu et al., 2016; Renault et al., 2019; Rai et al., 2021).

From a modeling perspective, there is a practical motivation to better understand and quantify how wind drives the ocean. While using absolute wind stress $\boldsymbol{\tau}_a$ overestimates wind work, Renault et al. (2018) showed that using formulations of relative wind stress $\boldsymbol{\tau}_r$ based on relative wind velocity $\mathbf{u}_r$ *underestimates* the wind work when the atmospheric response is absent in ocean-only models compared to fully coupled ocean-atmosphere models. Ocean-only simulations have been shown by Renault et al. (2018) to yield an exaggerated eddy killing effect, thereby yielding an under-energized eddy field. We shall show in this paper that an exaggerated eddy killing when using $\boldsymbol{\tau}_r$ can arise even in fully coupled atmosphere-ocean models if the atmospheric resolution is coarser than that of the ocean. To our knowledge, such spurious eddy killing due to resolution mismatch between the oceanic and atmospheric grids has not been recognized before. By deriving an analytic expression for wind-work as a function of length-scale at any geographic location, we are able to offer a simple reformulation of the bulk wind stress, which removes such spurious eddy killing in models with resolution mismatch. The reformulated stress yields very good agreement with satellite observations.

This paper is organized as follows. Section 2 is an overview of air-sea mechanical coupling at mesoscales. Section 3 discusses Reynolds Averaging and coarse-graining methods. Section 4 describes the datasets we use. Section 5 discusses wind work at large-scales and mesoscales using Reynolds Averaging and coarse-graining approaches. In section 6 we explain the air-sea mechanical coupling at different length-scales analytically, demonstrate it

with toy examples, and discuss the effects of resolution mismatch. Section 7 discusses implications on modeling and provides a recipe to fix the bias due to resolution mismatch. Section 8 discusses some of the limitations and practical choices made in this work. The paper concludes with a summary and discussion in section 9, followed by an appendix.

## 2 Air-Sea Mechanical Coupling

Wind work at the air-sea interface is the transfer of mechanical energy from wind to the ocean. Here, we focus on the multiscale nature of such transfer. The work done by wind on the geostrophic ocean is important as it is provides the energy needed for maintaining global circulation of the ocean (Munk & Wunsch, 1998). The transfer of this energy is given by

$$P = \boldsymbol{\tau} \cdot \mathbf{u}_o \ , \tag{1}$$

where $\boldsymbol{\tau}$ is the surface wind stress and $\mathbf{u}_o$ is the surface ocean current. $\boldsymbol{\tau}$ in eq. (1) is formulated using a bulk aerodynamic method (e.g. Kundu et al., 2015). Despite several works (Bye, 1985; Pacanowski, 1987; Dawe & Thompson, 2006; Duhaut & Straub, 2006) pointing to its lower accuracy, many simulations and analyses relied on an absolute wind stress formulation

$$\boldsymbol{\tau}_a = \rho_{air} C_d |\mathbf{u}_a| \mathbf{u}_a, \tag{2}$$

that was solely a function of wind velocity at the ocean surface, $\mathbf{u}_a$, without accounting for the ocean current. Here, $\rho_{air} \approx 1.2$ kg/m$^3$ is air density and $C_d = O(10^{-3})$ is the coefficient of drag (W. Large & Pond, 1981; W. G. Large et al., 1994). A physically more correct formulation is relative wind stress,

$$\boldsymbol{\tau}_r = \rho_{air} C_d |\mathbf{u}_a - \mathbf{u}_o| (\mathbf{u}_a - \mathbf{u}_o) \ , \tag{3}$$

which is based on the wind velocity relative to the ocean surface current, $\mathbf{u}_o$. Having $|\mathbf{u}_a| \gg |\mathbf{u}_o|$ on average had been a justification for using the simpler $\boldsymbol{\tau}_a$ in eq. (2). In fact, $\boldsymbol{\tau}_a$ is still being used to date in some models contributing to the climate model intercomparison project CMIP6, e.g. the CanESM5 model from the Canadian Centre for Climate Modelling and Analysis (Swart et al., 2019) and the AWI-CM model from the Alfred Wegener Institute (Semmler et al., 2017).

While $|\mathbf{u}_a| \gg |\mathbf{u}_o|$ on average, they can be comparable in strong ocean currents, leading to significant regional biases (Pacanowski, 1987). Moreover, the small change in the wind stress formulation fundamentally changes the atmosphere-ocean coupling at the mesoscales (Zhai & Greatbatch, 2007; Renault, Molemaker, McWilliams, et al., 2016). One of the results of this work tells us that eq. (2) yields a small net positive power input into the oceanic mesoscales smaller than 300 km. In contrast, eq. (3) leads to a significant net removal of energy from those scales (Rai et al., 2021) due to eddy-killing (Renault, Molemaker, Gula, et al., 2016).

We shall now recap the standard explanation of eddy-killing (Zhai & Greatbatch, 2007; Renault, Molemaker, McWilliams, et al., 2016). Fig. 1 shows a large-scale wind blowing over an ocean eddy. Since wind stress, $\boldsymbol{\tau}_r$, is proportional to wind velocity relative to the ocean ($\mathbf{u}_a - \mathbf{u}_o$ in eq. (3)), it induces small-scale oceanic imprints (variations) in the wind stress (Renault, Molemaker, McWilliams, et al., 2016; Zhai & Greatbatch, 2007). This wind stress forces half of the eddy positively (positive work) and the other half negatively (negative work or damping). The stress opposing the ocean surface current is larger than the stress that drives the ocean surface current resulting in negative wind work to the eddy and is called eddy-killing (Renault, Molemaker, McWilliams, et al., 2016).

Several studies have reported differing global estimates for eddy killing using various methods, ranging from -142 GW to 22 GW. The standard explanation of eddy killing by (Zhai & Greatbatch, 2007) suggests the wind work on eddies should be negative. However, many of the earlier investigations (e.g., Duhaut & Straub, 2006; Y. Xu & Scott, 2008;

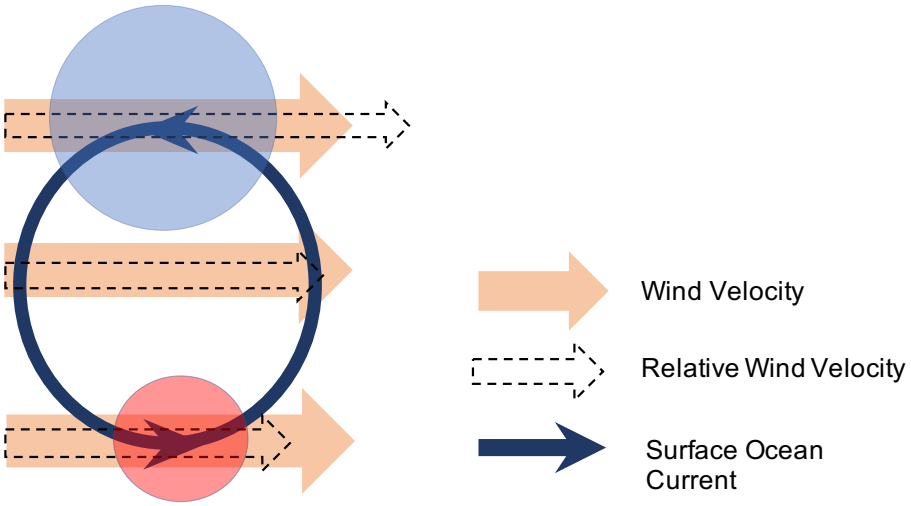


Figure 1: Standard explanation of eddy killing, which may be traced back to Zhai and Greatbatch (2007). A uniform (or large-scale) wind, $\overline{\mathbf{u}}_a$ acts on an ocean eddy (small-scale, $[\mathbf{u}_o]'_\ell$ ). The wind stress opposes (blue, negative work) the top half of the eddy and enhances (red, positive work) the bottom half. Since the stress exerted by the wind on the eddy is proportional to their relative velocity, the negative work dominates over the positive, resulting in the wind extracting energy from the eddy.

Hughes & Wilson, 2008; Hutchinson et al., 2010; Renault, Molemaker, Gula, et al., 2016) defined "eddy" as the temporal fluctuation, $\mathbf{u}'_o = \mathbf{u}_o - \langle \mathbf{u}_o \rangle$, around the time-mean $\langle \mathbf{u}_o \rangle$. Consistent with this definition, the measure of wind work on the eddy (i.e. fluctuating) field is $\langle \boldsymbol{\tau}_r \cdot \mathbf{u}'_o \rangle$ (note that $\langle \boldsymbol{\tau}_r \cdot \mathbf{u}'_o \rangle = \langle \boldsymbol{\tau}'_r \cdot \mathbf{u}'_o \rangle$). All these studies have found this quantity to be either positive or $\approx 0$ when integrated globally, suggesting a lack of eddy killing. For instance, $\langle \boldsymbol{\tau}_r \cdot \mathbf{u}'_o \rangle$ was found to be $\approx 9$ GW by Hughes and Wilson (2008) and $\approx 22$ GW by Scott and Xu (2009),

In order to reconcile expectations from the process in Fig. 1 with the miniscule values of $\langle \boldsymbol{\tau}_r \cdot \mathbf{u}'_o \rangle$, many investigations (e.g. Duhaut & Straub, 2006; Hughes & Wilson, 2008) often focused on the difference $P^{fluc}_{diff} = \langle \boldsymbol{\tau}_r \cdot \mathbf{u}'_o \rangle - \langle \boldsymbol{\tau}_a \cdot \mathbf{u}'_o \rangle$, which *is* negative. Duhaut and Straub (2006) reported that of the total reduction in wind work $\langle \boldsymbol{\tau} \cdot \mathbf{u}_o \rangle$ when using $\boldsymbol{\tau}_r$ versus $\boldsymbol{\tau}_a$, the eddy (fluctuating) component, $P^{fluc}_{diff}$, accounts for two thirds and the remaining one third is due to the mean flow. The scatterometry analysis of Hughes and Wilson (2008) showed the eddy (fluctuating) contribution to be even larger (over 75%) with $P^{fluc}_{diff} \approx$ -142 GW. The negative value of $P^{fluc}_{diff}$ is sometimes confused with eddy-killing depicted in Fig. 1.

While being of practical modeling significance, $P^{fluc}_{diff}$ is not a term that arises self-consistently within the "correct" dynamics itself, but is only a comparison between two manifestations of oceanic flow under different wind forcing. A negative $P^{fluc}_{diff}$ only implies that $\langle \boldsymbol{\tau}_r \cdot \mathbf{u}'_o \rangle < \langle \boldsymbol{\tau}_a \cdot \mathbf{u}'_o \rangle$. After all, it is possible to concoct numerous incorrect wind stresses other than $\boldsymbol{\tau}_a$ (e.g. with different drag coefficients) to use in a simulation and measure the difference in energy input relative to the "correct" dynamics. Therefore, $P^{fluc}_{diff}$ does not represent eddy-killing. The latter should arise self-consistently within a single manifestation (e.g. a simulation) of the dynamics. Indeed, the presence of eddy killing in the flow sketched in Fig. 1 does not rely on a comparison to another flow. The quantity $\langle \boldsymbol{\tau}_r \cdot \mathbf{u}'_o \rangle$ was found to be positive or negligibly small globally (Hughes & Wilson, 2008; Scott & Xu, 2009), which indicates that $\langle \boldsymbol{\tau}_r \cdot \mathbf{u}'_o \rangle$ is not the proper quantity to detect eddy killing.

More recently, C. Xu et al. (2016) pursued another approach to measure eddy killing by explicitly detecting eddies of size up to 400 km and found that wind work, $\boldsymbol{\tau}_r \cdot \mathbf{u}_o^{eddy}$, over such structures is $-27.7$ GW globally, where $\mathbf{u}_o^{eddy}$ is the velocity of detected eddies. Therefore, C. Xu et al. (2016) quantified the wind damping or killing of detected eddies. The work was very important in that it demonstrated eddy killing in the global ocean. The $-27.7$ GW eddy killing estimate represents a lower bound on the eddy killing taking place because it is restricted to vortical structures that satisfy certain criteria, for example closed flow loops that are sufficiently long-lived. Such criteria is ultimately subjective and excludes much of the remaining ocean flow.

Yet another approach to estimate eddy killing was developed in the form of a linear regression coefficient obtained from the correlation of (i) curl of wind stress and (ii) ocean surface vorticity (Seo et al., 2016; Renault, Molemaker, McWilliams, et al., 2016; Renault et al., 2017). Using the regression coefficient, Renault et al. (2017) estimated the global eddy killing to be $-48$ GW, while also using two other measures of eddy killing that yielded $-23$ GW and $-70$ GW in the same paper.

A first principles method for calculating wind work on eddies was presented in a recent study of ours (Rai et al., 2021). The method is based on deriving the dynamics at different length-scales using a coarse-graining approach, then measuring the wind work at those scales directly (see eq. (13)). This frees us from having to rely on empirical statistical correlations or on subjective criteria of what constitutes an eddy. Using altimetry data for the ocean surface current and QuikSCAT winds, Rai et al. (2021) found the wind work on geostrophic current of length-scale less than 260 km to be $-50$ GW, while being positive at larger scales. This indicates that scales smaller than 260 km are killed by wind on a global average. The eddy killing rate of $-50$ GW is significant and comparable to other energy pathway estimates, such as baroclinic and barotropic transfer of kinetic energy (Kang & Curchitser, 2015; Aluie et al., 2018; Yan et al., 2019). Rai et al. (2021) found that eddy killing has a clear seasonal cycle, peaking in winter. It was also observed that $\approx 70\%$ of eddy killing occurs in WBCs and the ACC, which cover a surface area that is merely $\approx 7\%$ of the global ocean. A main contribution of our present study is deriving a mathematical criterion for eddy killing to occur at any length-scale. This criterion provides the theoretical explanation for results in Rai et al. (2021) and shows that a mismatch in resolution between the atmosphere and ocean components of a GCM leads to an exaggeration of eddy-killing.

## 3 Methods

In this section, we summarize how to decompose the ocean flow as a function of length-scales using spatial coarse-graining (Buzzicotti et al., 2021). More detailed discussions of coarse-graining on a spherical surface can be found in previous works (Aluie et al., 2018; Aluie, 2019; Buzzicotti et al., 2021). We also recap Reynolds averaging, which decomposes the flow into a temporal mean and fluctuating components (Vallis, 2017). Within both approaches, we focus on wind work.

### 3.1 Reynolds Averaging

Reynolds averaging is a traditional approach to analyzing unsteady, eddying, or turbulent flows. It relies on *ensemble* averaging to decompose the *mean* from the *fluctuating* components of a field. Oftentimes, including in physical oceanography, ensemble averaging is replaced with time-averaging. For our purposes, the mean wind stress and ocean surface current are $\langle \boldsymbol{\tau} \rangle$ and $\langle \mathbf{u}_o \rangle$, respectively, where $\langle ... \rangle$ represents temporal average.

Within the Reynolds averaging framework, one can identify the energy input by the wind into the mean flow from its kinetic energy budget, $\partial_t \rho |\langle \mathbf{u}_o \rangle|^2/2 = \ldots$, where $\rho$ is surface density and $\partial_t$ is a time derivative (e.g., Vallis, 2017). This is the *Mean Power* input

(per unit area) into the mean flow:

$$MP^{Rey} = \langle \boldsymbol{\tau} \rangle . \langle \mathbf{u}_o \rangle \tag{4}$$

Superscript 'Rey' is used to indicate that this term arises from the Reynolds decomposition.

The remainder of the wind work is channeled due to the presence of a fluctuating part of the flow, often called "eddies." Such *Eddy Power* input (per unit area) is:

$$EP^{Rey} = \langle \boldsymbol{\tau} \cdot \mathbf{u}_o \rangle - \langle \boldsymbol{\tau} \rangle \cdot \langle \mathbf{u}_o \rangle, \tag{5}$$

which simplifies to

$$\langle \boldsymbol{\tau} \cdot \mathbf{u}_o \rangle - \langle \boldsymbol{\tau} \rangle \cdot \langle \mathbf{u}_o \rangle = \langle \boldsymbol{\tau}' \cdot \mathbf{u}_o' \rangle, \tag{6}$$

where

$$\boldsymbol{\tau}' = \boldsymbol{\tau} - \langle \boldsymbol{\tau} \rangle, \quad \text{and} \quad \mathbf{u}_o' = \mathbf{u}_o - \langle \mathbf{u}_o \rangle. \tag{7}$$

Eq. (6) is valid only due to an important property of Reynolds averaging: for any field $\phi$,

$$\langle \langle \phi \rangle \rangle = \langle \phi \rangle \implies \langle \phi' \rangle = \langle \phi - \langle \phi \rangle \rangle = 0. \tag{8}$$

It is important to bear in mind that this property depends on Reynolds averaging being a projection (Buzzicotti, Linkmann, et al., 2018). It does not hold in general for other decompositions, such as spatial coarse-graining (or filtering, see Germano (1992)) or running window time-averaging. A negative value for $EP^{Rey}$ indicates that wind is extracting energy from the "eddy" (fluctuating) component of the flow, *i.e.* it indicates eddy killing within the Reynolds averaging framework.

The *Total Power* input (per unit area) into the ocean is simply:

$$TP^{Rey} = \langle \boldsymbol{\tau} \cdot \mathbf{u_o} \rangle, \tag{9}$$

which follows from the time-averaged kinetic energy budget, $\langle \partial_t \rho |\mathbf{u}_o|^2/2 \rangle = \ldots$, irrespective of any decomposition.

The expression of $TP^{Rey}$ gives us some insight into why $EP^{Rey}$ as defined in eq. (5) rather than that in eq. (6), is the fundamental quantity of interest —it ensures that $EP^{Rey} + MP^{Rey} = TP^{Rey}$. The simplified expression in eq. (6) relies on the Reynolds averaging property $\langle \langle \phi \rangle \rangle = \langle \phi \rangle$ and is not generally true for other decompositions.

As demonstrated in recent studies (Buzzicotti et al., 2021; Storer et al., 2022), "mean" is not synonymous with "large length-scale." Similarly, "fluctuating" is not synonymous with "small-scale." It is generally expected that larger (smaller) scales tend to vary over longer (shorter) time-scales, but this is not always true. One counterexample is Rossby waves, which have a shorter time-scale at larger length-scales. Another is standing meanders or stationary eddies, such as the Mann eddy in the N. Atlantic, which have a small length-scale (relative to the gyre or basin) but are persistent in time. A proper length-scale decomposition that is independent of the temporal behavior of the flow is accomplished by spatial coarse-graining (e.g., Aluie & Kurien, 2011; Aluie et al., 2018; Srinivasan et al., 2019; Ryzhov et al., 2019; Khani et al., 2019).

### 3.2 Coarse Graining

For a field $\phi(\mathbf{x})$, a "coarse-grained" or (low-pass) filtered field, which contains length-scales larger than $\ell$, is defined as

$$\overline{\phi}_\ell(\mathbf{x}) = G_\ell * \phi, \tag{10}$$

where $*$ is a convolution on the sphere (Aluie, 2019) and $G_\ell(\mathbf{r})$ is a normalized kernel (or window function) so that $\int dS\ G_\ell(\mathbf{r}) = 1$, where $dS$ is the infinitesimal area measure on the sphere. Operation (10) may be interpreted as a local space average over a region of

diameter $\ell$ centered at point $\mathbf{x}$. Notice that $\overline{\phi}_\ell(\mathbf{x})$ has scale information $\ell$ as well as space information $\mathbf{x}$. The kernel

$$G_\ell(r) = A\,(0.5 - 0.5\tanh((|\mathbf{r}| - \ell/2)/10.0)) \tag{11}$$

we use, shown in Fig. 2, is essentially a graded Top-Hat kernel . The normalizing factor $A$ ensures $\int dS\ G_\ell(r) = 1$.

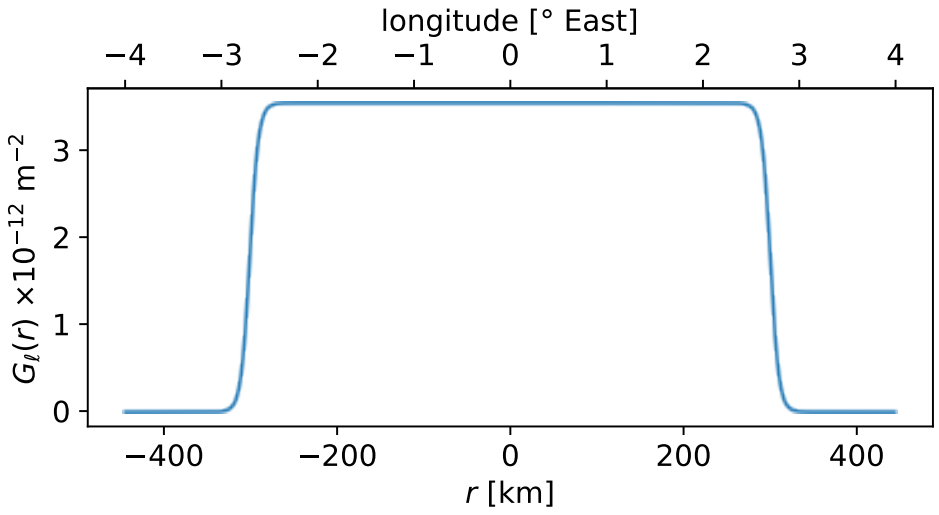


Figure 2: Kernel $G_\ell$ we use for coarse-graining is a Top-Hat filter with smoothed edges as defined in eq. (11). Distance $r = |\mathbf{r}|$ is geodesic (see eq.(7) in Buzzicotti et al. (2021)). In this figure, $\ell = 600$ km, although we probe a wide range of length-scales below using different values for $\ell$.

Unlike the Reynolds approach, which lacks control over the partitioning scale, coarse-graining allows for any choice of partitioning length-scale $\ell$. In the rest of our paper, we shall omit subscript $\ell$ whenever there is no risk of ambiguity.

Within the coarse-graining approach, large-scale wind stress and surface current are $\overline{\boldsymbol{\tau}}$ and $\overline{\mathbf{u}_o}$, respectively. One can identify the energy input by the wind into the large-scale flow (larger than $\ell$) from the kinetic energy budget, $\partial_t \rho |\overline{\mathbf{u}}_o|^2/2 = \ldots$ (e.g., Aluie et al., 2018). This is the wind work (per unit area) into oceanic scales larger than $\ell$:

$$MP^{Cg} = \overline{\boldsymbol{\tau}}\cdot\overline{\mathbf{u}_o}, \tag{12}$$

which is analogous to $MP^{Rey}$, with superscript 'Cg' to denote coarse-graining.

Similar to Eddy Power $EP^{Rey}$ from Reynolds averaging, the remainder of wind work is channeled due to the presence of scales smaller than $\ell$, which we shall also call "eddies." Whereas the "eddies" within the Reynolds averaging approach are *temporal* fluctuations relative to the time-mean, "eddies" within coarse-graining are *spatial* variations of length-scales smaller than $\ell$. Wind work (per unit area) into the small-scales ($< \ell$) is

$$EP^{Cg} = \overline{\boldsymbol{\tau}\cdot\mathbf{u}_o} - \overline{\boldsymbol{\tau}}\cdot\overline{\mathbf{u}_o}\ , \tag{13}$$

which is analogous to $EP^{Rey}$ in eq. (5).

Finally, the quantity corresponding to Total Power $TP^{Rey}$ from Reynolds averaging is

$$TP^{Cg} = \overline{\boldsymbol{\tau}\cdot\mathbf{u}_o}\ . \tag{14}$$

The reason $TP^{Cg}$ corresponds to the total wind work is because of the identity $\{\overline{\boldsymbol{\tau}\cdot\mathbf{u}_o}\} = \{\boldsymbol{\tau}\cdot\mathbf{u}\}$, where

$$\{\dots\} = \int dS\ (\dots) \tag{15}$$

is domain integration (Germano, 1992; Aluie, 2019).

A reader unfamiliar with the coarse-graining approach might have expected that wind work at small-scales is more naturally quantified by $(\boldsymbol{\tau}-\overline{\boldsymbol{\tau}})\cdot(\mathbf{u}_o-\overline{\mathbf{u}}_o)$. However, since coarse-graining does not generally satisfy $\overline{\overline{\phi}} = \overline{\phi}$ (Germano, 1992), unlike Reynolds averaging, identity (6) does not hold within the coarse-graining framework and one has to work with the more fundamental quantity, $EP^{Cg} = \overline{\boldsymbol{\tau}\cdot\mathbf{u}_o} - \overline{\boldsymbol{\tau}}\cdot\overline{\mathbf{u}_o}$. The sum $EP^{Cg} + MP^{Cg}$ yields total power $TP^{Cg}$, whereas $(\boldsymbol{\tau}-\overline{\boldsymbol{\tau}})\cdot(\mathbf{u}_o-\overline{\mathbf{u}}_o) + MP^{Cg}$ does not.

Another possible alternative to the definition of $EP^{Cg}$ in eq. (13) that may appear more natural is $\boldsymbol{\tau}\cdot\mathbf{u}_o - \overline{\boldsymbol{\tau}}\cdot\overline{\mathbf{u}_o}$. However, the budget in which this term arises is $\partial_t \frac{\rho}{2}(|\mathbf{u}_o|^2 - |\overline{\mathbf{u}}_o|^2) = \cdots$. While the quantity $\frac{\rho}{2}(|\mathbf{u}_o|^2 - |\overline{\mathbf{u}}_o|^2)$ may seem an adequate quantification for small-scale energy, it is not positive semi-definite *i.e.* it can have negative values (Vreman et al., 1994; Buzzicotti et al., 2021). This is why the appropriate small-scale kinetic energy within the coarse-graining framework (Germano, 1992; Vreman et al., 1994) is $\frac{\rho}{2}(\overline{|\mathbf{u}_o|^2} - |\overline{\mathbf{u}}_o|^2)$, which *is* guaranteed to be positive semi-definite if kernel $G_\ell \geq 0$ in eq. (10). It can be shown that this is a simple consequence of Jensen's inequality and convexity of the square operation, $\mathcal{F}(\mathbf{u}) = |\mathbf{u}|^2$, considering that $\overline{(\cdot)}$ is a (local) spatial average (Sadek & Aluie, 2018).

## 4 Description of Datasets

Geostrophic current ($\mathbf{u}_o$) data from AVISO Ssalto/Duacs daily sea level anomalies, which is distributed by Copernicus Marine Environment Monitoring Service (CMEMS), is used spanning the period of October 1999 to December 2006. It is a Level 4 processed dataset (gridded and blended) on a $0.25^\circ \times 0.25^\circ$ grid. This dataset includes estimates of geostrophic current along the equator, calculated using Lagerloef methodology (Lagerloef et al., 1999) with the $\beta$ plane approximation.

Level 3 processed QuikSCAT wind ($\mathbf{u}_{qs}$) measurements are available from the Physical Oceanography Distributed Active Archive Center (PODAAC). This data is in form of ascending (northward) and descending (southward) swaths and is gridded at $0.25^\circ \times 0.25^\circ$ resolution.

A satellite scatterometer such as the SeaWinds instrument on QuikSCAT is essentially a radar. The basic physical principle behind its operation is Bragg diffraction (or scattering), where the spacing between surface waves[3] is analogous to the lattice spacing in a crystal. The direct measurement from scatterometers is the radar cross-section (or backscatter coefficient) of surface waves, from which a model function allows the inference of wind stress magnitude and direction (Weissman et al., 1994; Stoffelen & Anderson, 1997). From wind stress, the equivalent wind velocity at 10 m above the sea surface is then retrieved under conditions of a neutrally stratified atmospheric boundary layer (Geernaert & Katsaros, 1986; Chelton et al., 2004). Such winds are often referred to as equivalent neutral stability winds (ENW). Since scatterometers are essentially stress-measuring instruments (Weissman et al., 1994), the derived wind velocity $\mathbf{u}_{qs}$ is that relative to the oceanic flow (Cornillon & Park, 2001; Kelly et al., 2001). Therefore, the wind velocity from scatterometer products, being a relative velocity, inherently includes the direct "imprint" of ocean surface currents, and arise from a fully coupled system in which the atmosphere responds dynamically to oceanic feedback.

[3] QuikSCAT's radar frequency was in the Ku-band to detect short surface gravity-capillary waves 1–2 cm in wavelength.

The second wind dataset ($\mathbf{u}_a$) is from the National Center for Environmental Prediction/Department of Energy (NCEP/DOE) Reanalysis 2 (R2) Project's daily surface wind dataset, available from the Earth System Research Laboratory (ESRL) (`https://www.esrl.noaa.gov/psd/`). The dataset for winds at 10 m above surface (interpolated from sigma levels) is available on a gaussian grid of $\approx 2^\circ \times 2^\circ$ resolution. We interpolate the data linearly onto a $0.25^\circ \times 0.25^\circ$ to match the wind dataset from QuikSCAT and the geostrophic current dataset from AVISO.

## 5 Comparing Decompositions and Wind Stress Formulations

This study builds upon our previous work on eddy killing (Rai et al., 2021). There, we used QuikSCAT winds and altimeter data to scan $EP^{Cg}$ as a function of length-scale, which showed that eddy killing acts at scales smaller than 260 km on a global average, extracting energy from the ocean at the rate of 50 GW.

In this section, we conduct a detailed comparison between the Reynolds averaging and coarse-graining decompositions, showing that the former does not capture eddy killing in a physically consistent manner. Motivated in part by how to best force oceanic circulation using winds in models, we also compare three different wind stress formulations,

1. QuickSCAT stress, $\boldsymbol{\tau}_{qs}$,
2. Absolute NCEP stress, $\boldsymbol{\tau}_a$,
3. Relative NCEP stress, $\boldsymbol{\tau}_r$.

We measure wind work done by these stresses on the large-scale flow via $MP$ in eq. (12), and on the mesoscale flow via $EP$ in eq. (13).

We show in this section that $\boldsymbol{\tau}_a$ yields no eddy killing at the mesoscales and overestimates energy input into the large-scale flow ($> 300$ km) by $\approx 10\%$ compared to $\boldsymbol{\tau}_{qs}$, which we use as our benchmark. We find that $\boldsymbol{\tau}_r$ inputs the correct amount (within $\approx 0.5\%$) of energy into the large-scale flow ($> 300$ km) on a global average. However, $\boldsymbol{\tau}_r$ *overestimates* mesoscale eddy killing by a factor of $\approx 4$ compared to $\boldsymbol{\tau}_{qs}$. The reason for this overestimate is resolution mismatch, which we discuss in the following sections 6 and 7.

Our results imply that the reduction in overall wind work when using $\boldsymbol{\tau}_r$ compared to $\boldsymbol{\tau}_a$ is not merely due to eddy killing, but also due to a reduction in wind work at large-scales. Our results here provide additional evidence to that in Rai et al. (2021) showing that WBCs are strongly forced positively by winds at large-scales. However, without a scale decomposition to disentangle eddy-killing at mesoscales, such wind forcing may appear weak.

### 5.1 Wind Stress Formulation

Wind work at different scales depends on the stress formulation. Here, we discuss the bulk formulations of wind stress, which are used in general circulation models.

We focus on the bulk parameterization (W. G. Large et al., 1994) to calculate wind stress. This parameterization is a bulk aerodynamic formula that uses the Monin–Obukhov similarity theory to calculate the coefficient of drag as a function of wind speed at 10 m from the ocean surface. Within the scope of this work, we focus on mechanical coupling between the ocean and atmosphere without considering heat fluxes explicitly. In other words, we assume that the W. G. Large et al. (1994) parameterization is sufficient to quantify wind work.

The bulk parameterization in W. G. Large et al. (1994) is commonly used in numerical models (e.g., Fu & Chao, 1997; Pei et al., 2022; Sui et al., 2022) and in studies of wind work on the ocean (e.g., Hughes & Wilson, 2008; Scott & Xu, 2009). The surface stress is a function of relative wind velocity $\mathbf{u}_r$,

$$\boldsymbol{\tau}_r = \mathbf{u}_r \, F(u_r) \ . \tag{16}$$

The scalar function $F(u_r)$ depends on the velocity magnitude $u_r = |\mathbf{u}_r|$ and is defined as

$$F(u_r) = \alpha + \beta u_r + \gamma {u_r}^2 \ . \tag{17}$$

The constants are $\alpha = 2.70 \times 10^{-3} \rho_{air}$ ($\mathrm{kg\,m^{-2}\,s^{-1}}$), $\beta = 1.42 \times 10^{-4} \rho_{air}$ ($\mathrm{kg\,m^{-3}}$), and $\gamma = 7.64 \times 10^{-5} \rho_{air}$ ($\mathrm{kg\,m^{-4}\,s}$). The air density used is $\rho_{air} = 1.223\,\mathrm{kg\,m^{-3}}$. Equation (16) is equivalent to equation (3). If the relative wind velocity $\mathbf{u}_r$ is replaced by absolute wind velocity $\mathbf{u}_a$, eq. (16) is equivalent to eq. (2).

Using eq. (16), we consider three different wind stress formulations, summarized in Table 1, along with a list of datasets used. The first wind stress we consider is based on absolute wind $\mathbf{u}_a$ using NCEP wind data, which replaces $\mathbf{u}_r$ in eq. (16). We shall denote this stress by $\boldsymbol{\tau}_a$ hereafter. This stress lacks information about the oceanic surface current, which leads to a lack of mesoscale eddy killing as we show below.

The second formulation incorporates the geostrophic ocean current $\mathbf{u}_o$ to define relative wind velocity, $\mathbf{u}_r = \mathbf{u}_a - \mathbf{u}_o$ in eq. (16). We shall denote this stress by $\boldsymbol{\tau}_r$ hereafter. Since the formulation $\boldsymbol{\tau}_r$ incorporates the ocean surface current, it is able to account for eddy killing. However, as we shall see, such eddy killing is highly exaggerated ($\approx \times 4$) due to the resolution mismatch between $\mathbf{u}_a$ and $\mathbf{u}_o$.

The third formulation uses QuikSCAT winds, $\mathbf{u}_{qs}$ instead of $\mathbf{u}_r$ in eq. (16). We shall denote this stress by $\boldsymbol{\tau}_{qs}$ hereafter. Since $\mathbf{u}_{qs}$ is derived from scatterometery, which essentially measures the ocean surface stress (Bourassa et al., 2003; Renault, Molemaker, McWilliams, et al., 2016), it represents the wind velocity relative to the ocean surface current (Cornillon & Park, 2001; Kelly et al., 2001). Therefore, $\boldsymbol{\tau}_{qs}$ is a relative wind stress formulation. We use this stress as our benchmark since it is physically the most accurate among the three formulations. Moreover, $\mathbf{u}_{qs}$ data has a spatial resolution similar to that of $\mathbf{u}_o$. Note that since the QuikSCAT data is originally along swaths, we perform a 7-day running average of $\boldsymbol{\tau}_{qs}$ to obtain global coverage. For consistency, we also perform a 7-day running average on $\mathbf{u}_o$, $\boldsymbol{\tau}_a$ and $\boldsymbol{\tau}_r$.

We use subscripts 'a', 'r' and 'qs' for the wind work quantities $MP$, $EP$, and $TP$ (in eqs. (4),(5),(9) or eqs. (12)-(14)) to indicate the respective stresses $\boldsymbol{\tau}_a$, $\boldsymbol{\tau}_r$ and $\boldsymbol{\tau}_{qs}$ used in their calculations. For instance, wind work on the temporally fluctuating flow within the Reynolds decomposition using $\boldsymbol{\tau}_{qs}$ is denoted by

$$EP^{Rey}_{qs} = \langle \boldsymbol{\tau}_{qs} \cdot \mathbf{u}_o \rangle - \langle \boldsymbol{\tau}_{\boldsymbol{qs}} \rangle \cdot \langle \mathbf{u}_o \rangle = \langle \boldsymbol{\tau}'_{qs} \cdot \mathbf{u}'_o \rangle \tag{18}$$

Similarly, wind work on the large-scale flow ($> \ell$) within the coarse-graining decomposition using $\boldsymbol{\tau}_r$ is denoted by

$$MP^{Cg}_{r} = \overline{\boldsymbol{\tau}}_r \cdot \overline{\mathbf{u}_o} \ . \tag{19}$$

We sometimes omit the subscript to denote wind work that is agnostic to the stress formulation.

## 5.2 Reynolds Averaging

### *5.2.1 Reproducing Prior Results*

Evaluating wind work within the Reynolds Averaging framework allows us to reproduce results from prior studies (Wunsch, 1998; Hughes & Wilson, 2008; Scott & Xu, 2009). These are summarized in Table 2 using the three stresses, $\boldsymbol{\tau}_a$, $\boldsymbol{\tau}_r$ and $\boldsymbol{\tau}_{qs}$.

The values of $TP^{Rey}$, $MP^{Rey}$ and $EP^{Rey}$ we obtain agree well with those from previous studies. From Table 2, comparing row 4a from our wind work estimates using $\boldsymbol{\tau}_a$, we see that each of $TP^{Rey}_a$, $MP^{Rey}_a$, and $EP^{Rey}_a$ are almost identical to those in row 1a from Scott

Table 1: Source and formulation of wind velocity, ocean velocity, and wind stress. Wind stress is obtained from the bulk formulation (W. Large & Pond, 1981; W. G. Large et al., 1994) using eq. (16) above.

| Row #. | symbol | Description | Formulation/Source | Remark |
|---|---|---|---|---|
| 1 | $\mathbf{u}_a$ | NCEP wind | NOAA | $\approx 2^\circ \times 2^\circ$ grid |
| 2 | $\mathbf{u}_{qs}$ | QuikSCAT wind | PO.DAAC | $0.25^\circ \times 0.25^\circ$ grid |
| 3 | $\mathbf{u}_o$ | Geostrophic ocean surface current | AVISO | $0.25^\circ \times 0.25^\circ$ grid |
| 4 | $\widetilde{\mathbf{u}_o}$ | Geostrophic ocean surface current coarsened to match the resolution of $\mathbf{u}_a$ | AVISO | filtered $\mathbf{u}_o$ with $2^\circ \times 2^\circ$ latlong boxcar kernel |
| 5 | $\boldsymbol{\tau}_a$ | NCEP absolute wind stress | $\mathbf{u}_a F(u_a)$ | This formulation is based on absolute wind velocity |
| 6 | $\boldsymbol{\tau}_r$ | NCEP relative wind stress | $(\mathbf{u}_a - \mathbf{u}_o)F(\lvert\mathbf{u}_a - \mathbf{u}_o\rvert)$ | This formulation is based on relative wind velocity. |
| 7 | $\boldsymbol{\tau}_{qs}$ | QuikSCAT wind stress | $\mathbf{u}_{qs}F(u_{qs})$ | This is our benchmark wind stress. It is inherently based on relative wind velocity. |
| 8 | $\boldsymbol{\tau}_{r2}$ | modified NCEP relative wind stress | $(\mathbf{u}_a - \widetilde{\mathbf{u}_o})F(\lvert\mathbf{u}_a - \widetilde{\mathbf{u}_o}\rvert)$ | This is a recipe for wind stress we propose to fix exaggerated eddy killing due to resolution mismatch. |

and Xu (2009). Our $EP_{qs}^{Rey}$ colormap in Fig. 3A is indistinguishable from Figure 4 in Scott and Xu (2009). Similarly, row 1b from Scott and Xu (2009) and row 4c from our wind work estimates using $\boldsymbol{\tau}_{qs}$, show excellent agreement. We are also able to reproduce results from Hughes and Wilson (2008) for the extra-equatorial ocean, which excludes the $\pm 3^\circ$ band (row 2b and row 4d in Table 2).

"Eddy" killing necessitates that $EP^{Rey} < 0$ within the Reynolds averaging approach in which "eddies" are defined as the temporal fluctuations. However, consistent with previous studies, we find that the wind feeds a net positive amount of energy to these "eddies." Using the QuikSCAT dataset, we measure $\{EP_{qs}^{Rey}\} = +44$ GW compared to the +42 GW value reported by Scott and Xu (2009). If we exclude the $\pm 3^\circ$ equatorial band as in Hughes and Wilson (2008), we measure $\{EP_{qs}^{Rey}\} = +13$ GW compared to their +9.3 GW. Scott and Xu (2009) also reported $EP_{qs}^{Rey}$ excluding the equator using a variety of datasets for wind stress and ocean currents; their values ranged from +1 GW to +62 GW, all being positive (see their Table 1). These independent results all seem to agree qualitatively that "eddies" (fluctuations) gain energy from the wind in the global budget rather than being killed – a

Table 2: Comparison of our wind work estimates from Reynolds Averaging and coarse-graining frameworks with previous studies. $\boldsymbol{\tau}_a*$ in row 1 from Hughes and Wilson (2008) does not use NCEP winds but a Taylor expansion of QuikSCAT winds to estimate absolute wind velocity. Hughes and Wilson (2008) used data from Oct-1999 to Oct-2006 and omitted some regions (e.g. ice-covered) with fewer than 100 instances of data as well as the latitude band of $\pm 3^\circ$ latitude. (Scott & Xu, 2009) used the data from year 2000 to 2005 and omitted the some regions with fewer than 52 instances of data

| Row # | | Study/Paper | $\boldsymbol{\tau}$ used | $TP^{Rey}$ or $TP^{Cg}$ [GW] | $MP^{Rey}$ or $MP^{Cg}$ [GW] | $EP^{Rey}$ or $EP^{Cg}$ [GW] | Remarks |
|---|---|---|---|---|---|---|---|
| 1 | a | (Scott & Xu, 2009) | $\boldsymbol{\tau}_a$ | 1100 | 980 | 120 | row 8 in their table 1 |
| | b | | $\boldsymbol{\tau}_{qs}$ | 920 | 878 | 42 | row 5 in their table 1 |
| 2 | a | (Hughes & Wilson, 2008) | $\boldsymbol{\tau}_a*$ | 950 | | | extra equatorial |
| | b | | $\boldsymbol{\tau}_{qs}$ | 760 | 751 | 9 | extra equatorial |
| 3 | | (Wunsch, 1998) | $\boldsymbol{\tau}_a$ | 880 | 841 | 39 | extra equatorial |
| 4 | a | Our Estimation from Reynolds Averaging | $\boldsymbol{\tau}_a$ | 1104 | 978 | 126 | global coverage, includes ice covered area |
| | b | | $\boldsymbol{\tau}_a$ | 902 | 821 | 81 | extra-equatorial, neglected ice covered regions |
| | c | | $\boldsymbol{\tau}_{qs}$ | 920 | 876 | 44 | global coverage, includes ice covered area |
| | d | | $\boldsymbol{\tau}_{qs}$ | 760 | 747 | 13 | extra-equatorial, neglected ice covered regions |
| | e | | $\boldsymbol{\tau}_r$ | 788 | 892 | -103 | global coverage, includes ice covered area |
| 5 | a | Our Estimation from Coarse Graining | $\boldsymbol{\tau}_a$ | 1104 | 1083 | 22 | filtered at $\ell = 300\ km$, global coverage, includes ice covered area |
| | b | | $\boldsymbol{\tau}_{qs}$ | 920 | 969 | -49 | filtered at $\ell = 300\ km$, global coverage, includes ice covered area |
| | b | | $\boldsymbol{\tau}_r$ | 788 | 974 | -186 | filtered at $\ell = 300\ km$, global coverage, includes ice covered area |

shortcoming of the meaning of "eddy" within the Reynolds averaging approach as we shall discuss below (see also Rai et al. (2021)).

The small quantitative differences among the three studies may be attributed to the following: (i) Hughes and Wilson (2008) use only ascending passes of QuikSCAT, while we use both ascending and descending, (ii) Scott and Xu (2009) regrid their data onto a $1/3^\circ$ grid while our data is on a $1/4^\circ$ grid, (iii) we use the same mask to exclude unavailable data such as due to seasonal ice coverage, while Hughes and Wilson (2008) use a time-varying mask, and Scott and Xu (2009) use estimates from other sources to fill in the missing data. Results from Wunsch (1998) (row 3 in Table 2) are also consistent but show more significant quantitative differences, which is probably due to the older altimetry and reanalysis products used.

#### *5.2.2 Role of Stress Formulations*

We now delve into comparing wind work estimates from the different stress formulations, $\boldsymbol{\tau}_a$, $\boldsymbol{\tau}_r$ and $\boldsymbol{\tau}_{qs}$. Fig. 3 shows that values of $EP^{Rey}$ are quite sensitive to the stress formulation, whereas $MP^{Rey}$ in Fig. 4 (and $TP^{Rey}$ in Fig. A1 in the appendix) seems relatively insensitive. Indeed, the colormaps of $MP_a^{Rey}$, $MP_r^{Rey}$, $MP_{qs}^{Rey}$ in Fig. 4 are almost indistinguishable. Since most of the $TP^{Rey}$ contribution is from Mean Power input $MP^{Rey}$, colormaps of $TP_a^{Rey}$, $TP_r^{Rey}$, $TP_{qs}^{Rey}$ in Fig. A1 are also indistinguishable.

A closer look at wind work in Table 2 estimated from $\boldsymbol{\tau}_a$ (row 4a) versus $\boldsymbol{\tau}_r$ (row 4e) reveals significant quantitative differences in both $TP^{Rey}$ and $MP^{Rey}$, in addition to the qualitative difference in $EP^{Rey}$. We can see that $TP_r^{Rey}$ is smaller than $TP_a^{Rey}$ by $\approx 30\%$ (or 316 GW), in agreement with estimates by Duhaut and Straub (2006). The dominant reduction is due to differences in $EP^{Rey}$ (229 GW difference between rows 4a and 4e in Table 2), which measures the wind work on the temporally fluctuating ocean currents. However, the most physically accurate formulation $\boldsymbol{\tau}_{qs}$ yields $EP_{qs}^{Rey} > 0$, consistent with previous studies (Hughes & Wilson, 2008; Scott & Xu, 2009). While it is well appreciated in the community that absolute wind stress formulations ($\boldsymbol{\tau}_a$) overestimate wind work and over-energize the ocean circulation, we shall show below that relative stress formulations ($\boldsymbol{\tau}_r$) can be just as erroneous in the opposite direction, by removing too much energy from the ocean due to resolution mismatch.

It is obvious from Fig. 3 that values of Eddy Power input $EP^{Rey}$ are especially sensitive to the stress used. For example, in strongly eddying regions, such as WBCs, $EP_a^{Rey}$ using NCEP absolute wind stress shows in Fig. 3C a dominance of positive values, whereas $EP_r^{Rey}$ using NCEP relative wind stress in Fig. 3E shows a dominance of negative values, indicating exaggerated "eddy" killing. Values for $EP_{qs}^{Rey}$ in Fig. 3A using QuikSCAT wind stress, which is the most physical, generally lie in-between $EP_a^{Rey}$ and $EP_r^{Rey}$.

### 5.3 Limitations of Reynolds Averaging

Estimates from Reynolds averaging (row 4 of Table 2 and Fig. 3) reveal no straightforward information about eddy killing. In fact, wind work on the temporally fluctuating ocean flow using the most accurate formulation of wind stress, $\boldsymbol{\tau}_{qs}$, is positive, suggesting a lack of eddy-killing. Definition of $EP^{Rey}$ in eq. (5) and its simplification in eq. (6) shows that $EP^{Rey}$ is a covariance between wind stress fluctuations, $\boldsymbol{\tau}'$, and "eddies" (ocean fluctuations), $\mathbf{u}'_o$. A negative covariance results from an anti-correlation between two signals. Therefore, a negative $EP^{Rey}$ requires that $\boldsymbol{\tau}'$ and "eddies" be anti-correlated *in time*.

The quantity $EP^{Rey}$ inherently relies on temporal fluctuations. It cannot account for the process depicted in Fig. 1 in which eddy killing is due to a stationary configuration. While most eddy killing in the real ocean is probably from transient rather than stationary "eddies," this example highlights the flaw inherent in $EP^{Rey}$. Compounding the problem with $EP^{Rey}$ are strong positive correlations between $\boldsymbol{\tau}'$ and $\mathbf{u}'_o$ in the tropics and the Indian

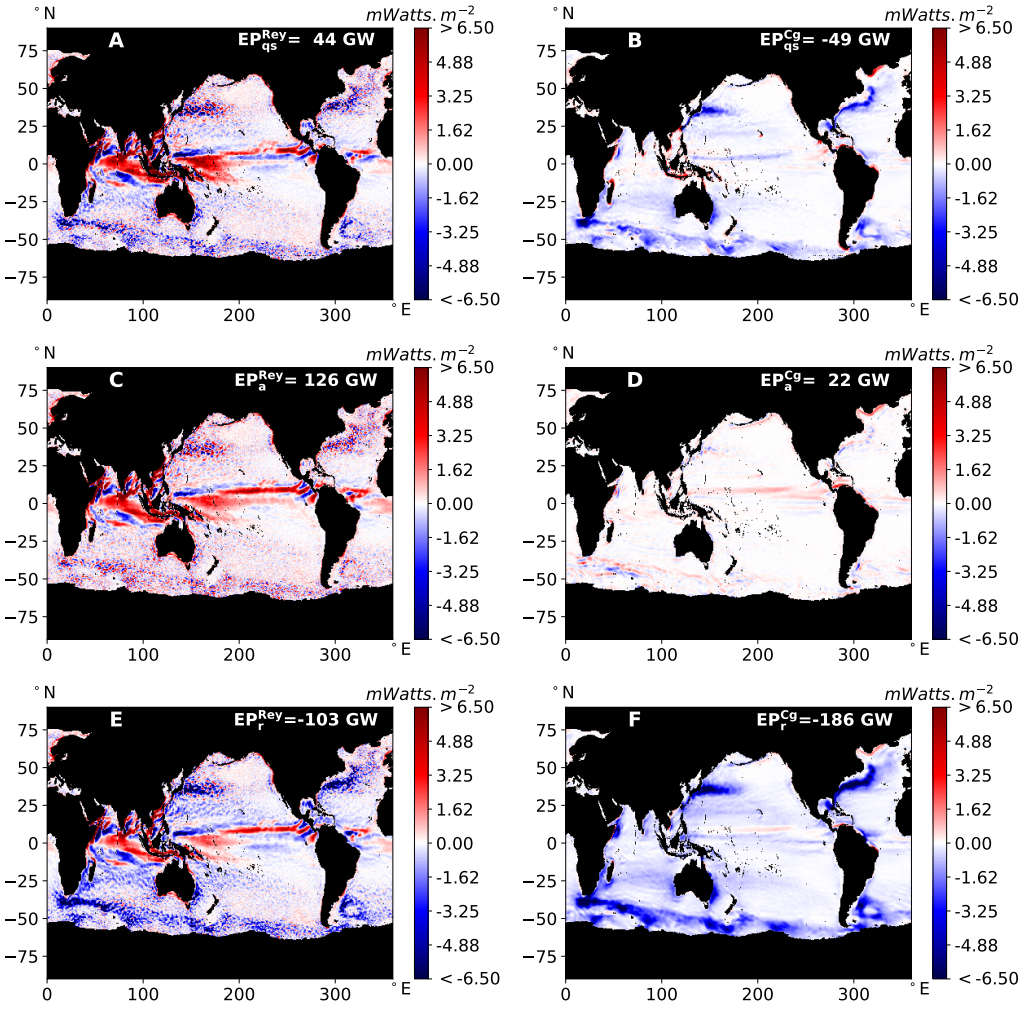


Figure 3: Wind work on "eddies" (in mW/m$^2$) within the Reynolds averaging framework ($EP^{Rey}$, left column) and coarse-graining at $\ell = 300$ km ($EP^{Cg}$, right column). Different rows show the three stress formulations: QuikSCAT stress $\boldsymbol{\tau}_{qs}$ (top), NCEP absolute stress $\boldsymbol{\tau}_a$ (middle), NCEP relative stress $\boldsymbol{\tau}_r$ (bottom). Each panel shows (top right corner) the global integral of wind work (see also Table 2, rows 4 and 5). Stark differences appear (i) between Reynolds (left) and coarse-graining (right) decompositions, and (ii) between different stress formulations in the three rows. $\boldsymbol{\tau}_{qs}$ is physically the most complete and accurate, whereas $\boldsymbol{\tau}_a$ ($\boldsymbol{\tau}_r$) overestimates (underestimates) wind work. Comparing $EP^{Rey}_{qs}$ in panel A to $EP^{Cg}_{qs}$ in panel B, we observe that coarse-graining is able to clearly detect eddy killing (negative values) throughout the ocean, especially in WBCs and the ACC, whereas Reynolds averaging in panel A yields sporadic values of mixed sign without a clear indication of eddy killing. The two decompositions differ starkly in the tropics, where we see pronounced positive values in panel A that are absent in panel B, due to the fundamental difference between the two on the meaning of an "eddy". We also see obvious differences between the stress formulations: absolute stress $\boldsymbol{\tau}_a$ (middle row), which spuriously inflates the wind power fed into the ocean, including the eddies, is biased to more positive values, with barely any eddy killing noticeable, while relative stress $\boldsymbol{\tau}_r$ (bottom row), shows a bias toward negative values, indicating exaggerated eddy killing.

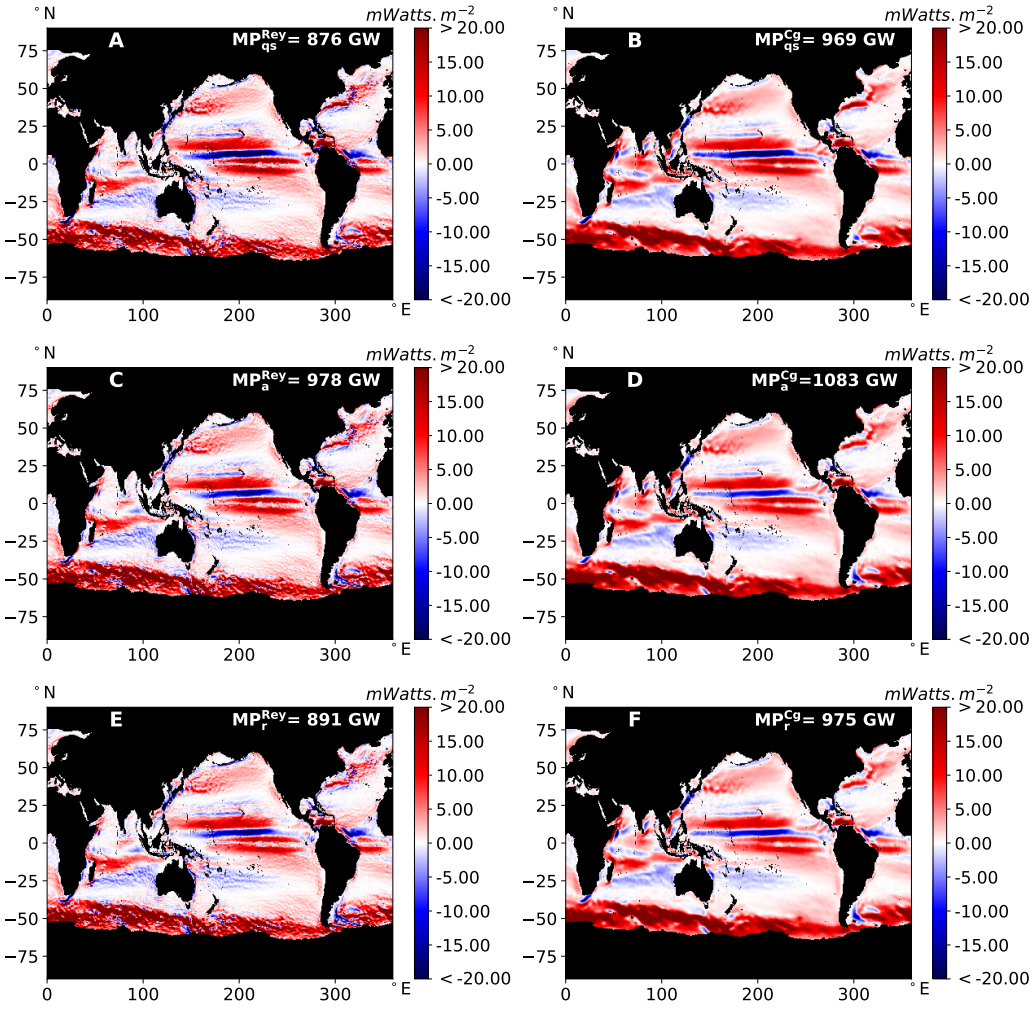


Figure 4: Similar to Fig. 3, but shows wind work (in W/m$^2$) on the time-mean flow (left column) and large-scale ($>$ 300 km) flow (right column). Strong wind forcing is seen in WBCs, the equatorial currents, and the ACC using either $MP^{Rey}$ or $MP^{Cg}$. In contrast to Fig. 3, all six panels are qualitatively similar and are consistent with Table 2. Comparing panels D and F, we see that wind work due to $\boldsymbol{\tau}_a$ is slightly greater than that due to $\boldsymbol{\tau}_r$.

Ocean (see Fig. 3), even though these oceanic fluctuations are quite large in length-scale, likely associated with Rossby wave dynamics rather than mesoscale eddies in the traditional sense. As we've mentioned earlier, excluding the equatorial region still yields a positive, albeit smaller, $EP^{Rey}$ from our analysis and also from previous studies (Hughes & Wilson, 2008; Scott & Xu, 2009) . These biases are absent from the coarse-graining analysis (compare Figs. 3A and 3B), which we shall now discuss.

### 5.4 Coarse Graining

Within the coarse-graining framework, we analyzed the wind Total Power input, $TP^{Cg}$ in eq. (14), and its partitioning into scales larger than $\ell$, $MP^{Cg}$ in eq. (12), and into the "eddies" (scales $< \ell$), $EP^{Cg}$ in eq. (13). Again, we use subscripts '$qs$' ,'$a$' and '$r$' to distinguish the stress formulations in Table 1. Values of wind-work, when partitioned at

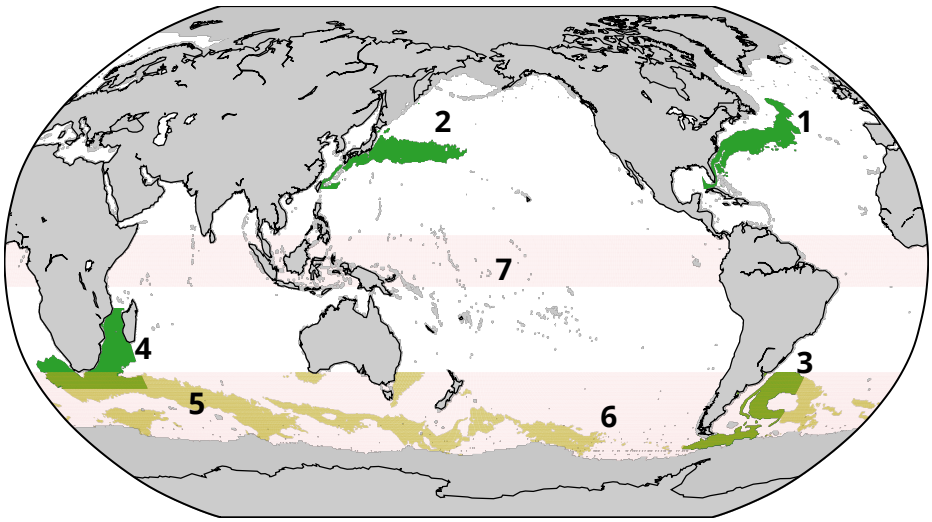


Figure 5: Regional masks. Regions 1, 2, 3, and 4 (green) are the Gulf Stream, Kuroshio Extension, Brazil Malvinas current and Agulhas current. Region 5 (yellow) is the ACC. Regions 6 and 7 (pink) are zonal bands representing the Southern Ocean and the Equatorial band. Regions 3 and 4 are overlapping with region 5 and 6. Region 5 is completely inside region 6. Grey regions lack data in some or all instances of time due to ice, rain (in QuikSCAT) or landmass. These regional masks are identical to those in (Rai et al., 2021). To see how these masks are defined, see Appendix B below .

$\ell = 300$ km, are summarized in Table 2, row 5. These values are simply obtained from spatially integrating the global maps in Figs. 3, 4, A1 (right columns).

#### *5.4.1 Power Input into Large Scales*

Fig. 4 shows that maps of $MP^{Cg}$ evaluated at $\ell = 300$ km are very similar to their counterparts from Reynolds averaging , $MP^{Rey}$, regardless of the stress formulation. Comparing Figs. A1 and 4 shows that the Total Power input into the ocean, $TP^{Cg}$, is mostly deposited at large-scales ($> 300$ km) via $MP^{Cg}$. Maps of $MP^{Cg}$ themselves are also very similar to their Reynolds averaging counterparts, $MP^{Rey}$, regardless of the stress formulation. Therefore, to leading order, it appears that wind work on mean/large-scale flow is consistent between the Reynolds averaging and coarse-graining approaches. However, quantitative differences not immediately obvious from the colormaps in Figs. 4, A1, do exist. These can be seen in Table 2 by comparing $MP^{Rey}$ (row 4) to $MP^{Cg}$ (row 5), which shows discrepancies of $\approx 10\%$. Note that we necessarily have $TP^{Rey} = TP^{Cg}$ when integrated globally.

Differences due to the wind stress formulations can be seen in Table 2 (row 5), which shows that $MP_r^{Cg} < MP_a^{Cg}$ on a global average. This indicates that wind work on the large-scale currents decreases by $\approx 10\%$ when using $\boldsymbol{\tau}_r$ versus $\boldsymbol{\tau}_a$.

Differences between Reynolds averaging and coarse-graining and differences due to various stress formulations are quite stark when examining wind power fed into the mesoscales, as we shall now discuss.

#### *5.4.2 Power Input into Mesoscales*

Focusing on the QuikSCAT dataset analysis in Fig. 3B, we find that $EP_{qs}^{Cg}$ evaluated at $\ell = 300$ km has negative values in eddying regions in accord with the physical expectations

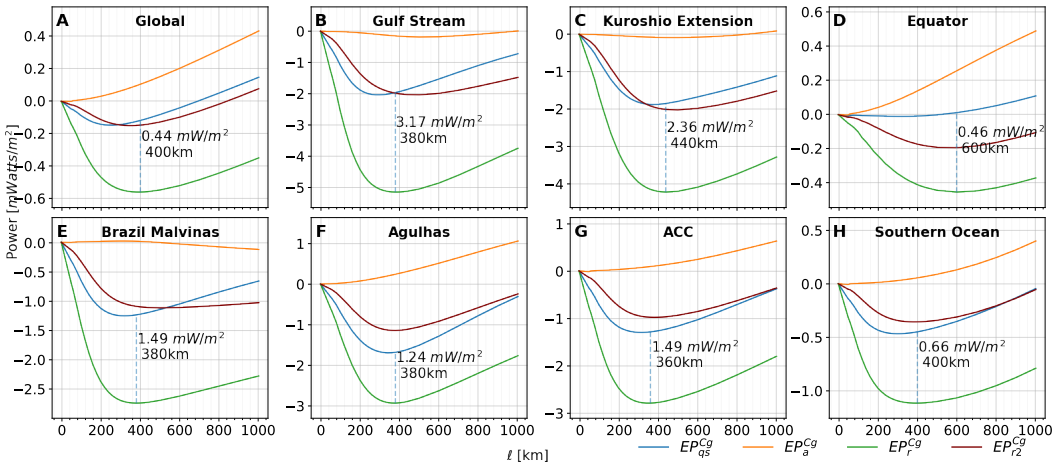


Figure 6: Performing a "scan" of $EP^{Cg}$ to quantify wind work over an entire range of length-scales. Plots are time-averaged and area-integrated over the regions in Fig. 5. $EP^{Cg}$ from $\boldsymbol{\tau}_a$ (orange), $\boldsymbol{\tau}_r$ (green), $\boldsymbol{\tau}_{qs}$ (blue), and $\boldsymbol{\tau}_{r2}$ (maroon) show the differences in wind work on mesoscales due to the different wind stress formulations. $\boldsymbol{\tau}_{r2}$ is a reformulation of $\boldsymbol{\tau}_r$ to correct its bias and is discussed later, in section 7.1. $EP^{Cg}_a$ is near zero or positive for all the regions because $\boldsymbol{\tau}_a$ cannot cause eddy killing but $EP^{Cg}_{qs}$, $EP^{Cg}_r$ and $EP^{Cg}_{r2}$ have negative values showing the stress $\boldsymbol{\tau}_{qs}$, $\boldsymbol{\tau}_r$ and $\boldsymbol{\tau}_{r2}$ cause eddy killing. $EP^{Cg}_r$ is more negative than $EP^{Cg}_{qs}$ because of spurious eddy killing from resolution mismatch. The vertical dashed blue line shows the magnitude and scale of excess eddy-killing in $EP^{Cg}_r$ relative to $EP^{Cg}_{qs}$. Such spurious eddy killing is 0.44 mW/m$^2$ for the global average (panel A), which integrates to $\approx$ 150 GW, showing that eddy killing by $\boldsymbol{\tau}_r$ is approximately 4$\times$ the eddy killing by $\boldsymbol{\tau}_{qs}$. This spurious eddy killing is stronger in WBCs and the ACC. In all panels, plots of $EP^{Cg}_{qs}$ and $EP^{Cg}_r$ are roughly parallel for $\ell$ larger than the length-scale indicated by the vertical blue dashed. This implies that wind work at those larger scales by $\boldsymbol{\tau}_r$ and $\boldsymbol{\tau}_{qs}$ is comparable. Plots of $EP^{Cg}_{r2}$ show that the stress reformulation we propose in section 7.1 corrects the spurious eddy killing bias.

as sketched in Fig. 1. Integrating the values in Fig. 3B over the global ocean, yields that the wind extracts energy from "eddies" (*i.e.* length-scales $<$ 300 km) at an average rate of -49 GW. This is consistent with our previous results in Rai et al. (2021), where we partitioned the flow at 260 km, the scale below which eddy-killing occurs.

Qualitative differences between Reynolds averaging and coarse-graining are apparent from the colormaps of wind power fed to the "eddies" in Fig. 3. Comparing the QuikSCAT coarse-graining analysis in Fig. 3B to the corresponding Reynolds averaging analysis in Fig. 3A, we see that the positive values there are mostly absent from Fig. 3B, especially in the tropics and in the Indian Ocean. Eddy killing ($EP^{Cg}_{qs} < 0$) is pronounced in WBCs and the ACC. From Reynolds averaging, these regions in Fig. 3A exhibit sporadic $EP^{Rey}_{qs}$ values of mixed sign without an obvious indication of eddy killing. Positive values of $EP^{Cg}_{qs}$ are mostly localized near land, where we expect winds and small-scale currents to be positively correlated since these currents are mostly wind-driven (Hughes & Wilson, 2008; Scott & Xu, 2009; Renault, Molemaker, McWilliams, et al., 2016).

### *5.4.3 Stress Formulations and Mesoscale Power Input*

Differences due to the wind stress formulations, which we had observed from Reynolds averaging also appear within the coarse-graining analysis, and for the same reasons. We

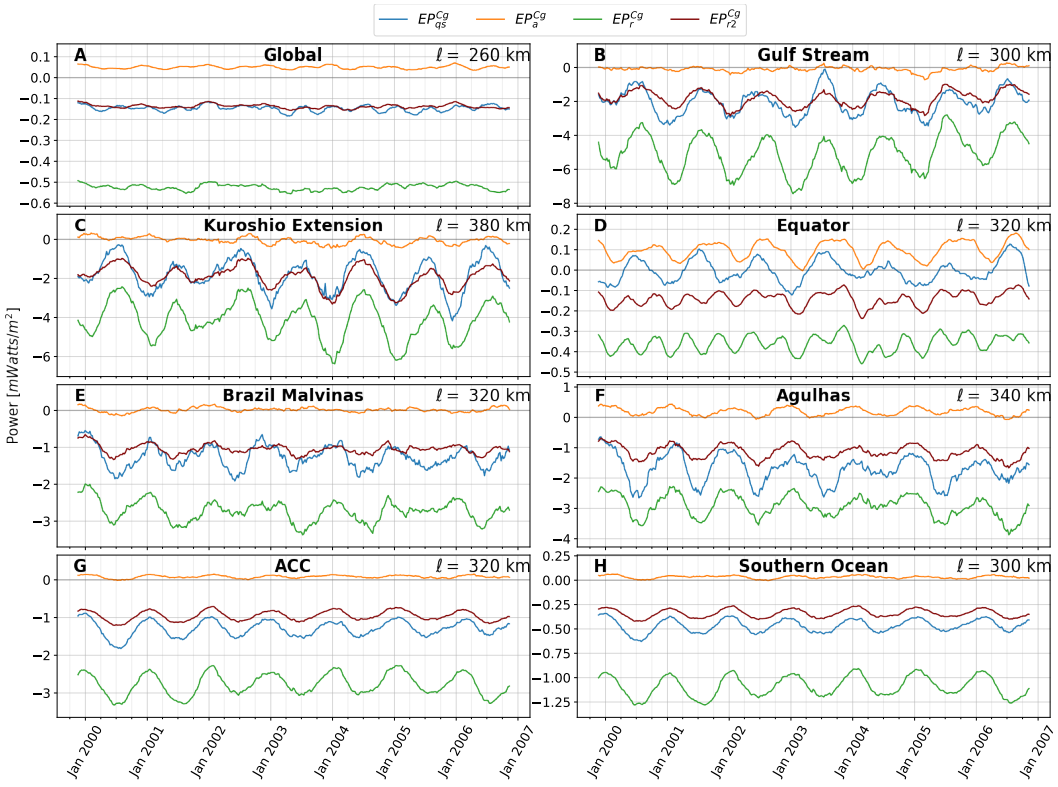


Figure 7: Time series of wind work at scales smaller than $\ell$ indicated in each panel (top-right corner). The choice of $\ell$ is that at which $EP_{qs}^{Cg}$ is minimum as a function of scale (Fig. 3 in Rai et al. (2021)). Plots of $EP_{qs}^{Cg}$ (blue), $EP_{a}^{Cg}$ (orange), $EP_{r}^{Cg}$ (green), $EP_{r2}^{Cg}$ (maroon) are area-integrated over the regions in Fig. 5 and use a 13 weeks running average. We see clear seasonlaity in $EP^{Cg}$, which is most negative in winter, indicating a peak in eddy-killing. In comparison, $EP_{a}^{Cg}$ is near-zero or negligibly positive because $\boldsymbol{\tau}_a$ cannot cause eddy-killing, while $EP_{qs}^{Cg}$ and $EP_{r}^{Cg}$ are always negative except for $EP^{qs}$ at the equator. $EP_{r}^{Cg}$ is more negative than $EP^{qs}$ due to spurious eddy killing by $\boldsymbol{\tau}_r$. With corrected wind stress $\boldsymbol{\tau}_{r2}$ (see section 7.1), we see from $EP_{r2}^{Cg}$ that the spurious eddy killing is removed and values of wind work are approximately equal to those of $EP_{qs}^{Cg}$.

see that when using NCEP absolute wind stress (Fig. 3D), $EP_{a}^{Cg}$ is biased to more positive values, with barely any eddy killing noticeable. Table 2 (row 5) also shows that $EP_{a}^{Cg} > 0$ on a global average, indicating that $\boldsymbol{\tau}_a$ is incapable of killing eddies, which is consistent with physical expectations. On the other hand, $EP_{r}^{Cg}$ using NCEP relative wind stress (Fig. 3f) shows a bias toward negative values, indicating exaggerated eddy killing. Indeed, table 2 (row 5) shows that $EP_{r}^{Cg} \approx 4 \times EP_{qs}^{Cg}$ on a global average. Since $\boldsymbol{\tau}_{qs}$ relies on the physically most complete stress measurement, we consider $EP_{qs}^{Cg}$ as our "truth."

By increasing the coarse-graining scale from $\ell = 0$ to $\ell \to \infty$, we expect $\{EP^{Cg}\}(\ell = 0) = 0$ to reach the total wind-work (a positive value) at very large filtering scales $\ell$. However, as we showed in Rai et al. (2021), a non-monotonic increase in $\{EP^{Cg}\}(\ell)$ with increasing $\ell$ can be an indication of eddy-killing at scales $< \ell$. This dip to negative values is seen in plots of $EP_{qs}^{Cg}(\ell)$ in Fig. 6 (also Fig. 3 in Rai et al. (2021)), which occurs globally and in all regions but the equator. These oceanic regions are shown in Fig. 5. The minimum value of $\{EP^{Cg}\}(\ell)$ yields the magnitude of eddy killing while the length-scale $\ell$ at which the minimum is attained yields informs us that all scales $< \ell$ are being killed by wind. The

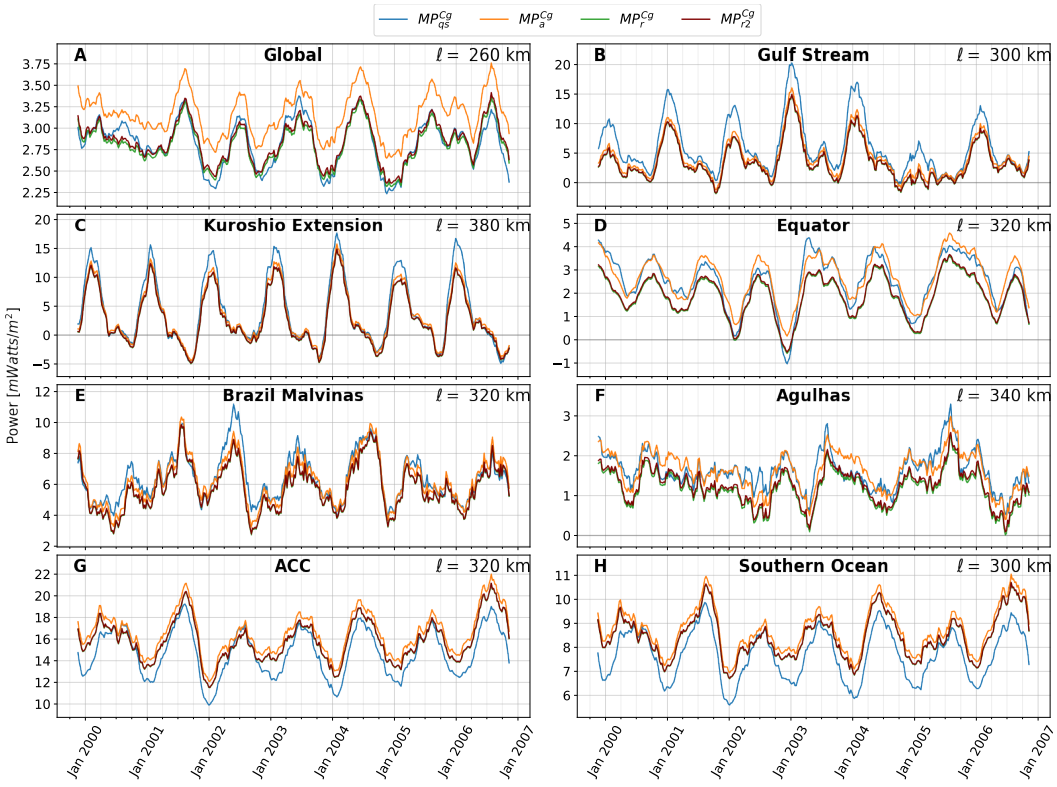


Figure 8: Similar to Fig. 7 but for $MP^{Cg}$, showing wind work at large-scales. $MP^{Cg}$ has seasonality with a peak during the local winter of the region. Unlike the plots of $EP^{Cg}$ the plots of $MP^{Cg}$ from all stresses are close to each other. This shows that the wind work at large-scales from all stress formulations is qualitatively similar. Plot of $MP^{Cg}_{r2}$ lie exactly over $MP^{Cg}_{r}$ in all regions (maroon plots overlay green plots almost exactly), which indicates that our reformulated stress $\boldsymbol{\tau}_{r2}$ (section 7.1) corrects the spurious eddy killing without affecting wind work at large-scales.

length-scale of eddy killing varies slightly among the various regions as discussed in Rai et al. (2021). The purpose of Fig. 6 is to show differences in $\{EP^{Cg}\}(\ell)$ due to the three stress formulations.

Fig. 6 shows stark differences among $EP^{Cg}_{qs}$, $EP^{Cg}_{a}$, and $EP^{Cg}_{r}$ that are consistent with those we observed from Fig. 3 at a $\ell = 300$ km. In Fig. 6A, we see that $EP^{Cg}_{a}$ increases monotonically with increasing $\ell$ or remains approximately zero, without dipping to negative values. Since $EP^{Cg}(\ell)$ is measure of the cumulative wind work on scales $< \ell$, a monotonic increase in $EP^{Cg}_{a}(\ell)$ over a range of $\ell$ indicates that $\boldsymbol{\tau}_a$ is energizing those scales. The monotonic increase is observed in all regions in Fig. 6, with the exception of the Gulf Stream, Kuroshio, and Brazil Malvinas showing slight negative values that are negligible and are probably due to recirculation patterns in the WBCs. Note that at small scales $< 200$ km, $EP^{Cg}_{a}(\ell) \approx 0$ in all panels of Fig. 6 and only starts increasing significantly at larger scales. This indicates that there is negligible work done by $\boldsymbol{\tau}_a$ on scales $< 200$ km, which is due to the NCEP wind resolution as we shall discuss later. It is expected that $\boldsymbol{\tau}_a$ is incapable of killing eddies (Duhaut & Straub, 2006; Zhai & Greatbatch, 2007).

In contrast to $EP^{Cg}_{a}$, Fig. 6A shows that $EP^{Cg}_{r}$ dips to negative values that are significantly below those attained by $EP^{Cg}_{qs}$. Moreover, we notice that the minimum of $EP^{Cg}_{r}$ is

shifted to slightly larger scales compared to the minimum of $EP_{qs}^{Cg}$. Fig. 6A shows a vertical blue dashed line at scale $\ell$ where $EP_{r}^{Cg}$ is minimum, which highlights the quantitative difference between $EP_{r}^{Cg}$ and $EP_{qs}^{Cg}$ at that scale. Comparing plots of $EP_{r}^{Cg}$ and $EP_{qs}^{Cg}$ from other regions in Fig. 6 shows the same trend. These indicate that $\boldsymbol{\tau}_r$ leads to a significant exaggeration of eddy killing ($\approx 4\times$) and also kills scales slightly larger than those killed by our benchmark $\boldsymbol{\tau}_{qs}$. At scales larger than $\approx 600$ km, we see that $EP_{r}^{Cg}$ and $EP_{qs}^{Cg}$ have similar slopes, which indicates that the wind work done by $\boldsymbol{\tau}_r$ and $\boldsymbol{\tau}_{qs}$ is similar at scales $> 600$ km. In summary, while $\boldsymbol{\tau}_r$ exaggerates the removal of energy at the mesoscales, it drives larger scales in a reasonably accurate manner.

Fig. 7 shows that differences in wind work on the mesoscales done by $\boldsymbol{\tau}_{qs}$, $\boldsymbol{\tau}_a$ and $\boldsymbol{\tau}_r$, which we discussed above, hold at all times and not just on average. Time-series of $EP_{qs}^{Cg}$ shows the seasonal cycle of eddy killing on the mesoscales (Rai et al., 2021), which occurs at all times and peaks in the local winter of all regions but the equator. Plots of $EP_{r}^{Cg}$ show the same seasonal behavior but with much exaggerated eddy-killing levels. In contrast, plots of $EP_{a}^{Cg}$ show negligible wind work, which is slightly positive on a global average in Fig. 7a, and with a muted seasonal cycle.

Fig. 8 shows the complementary $MP^{Cg}$, which measures wind work on all scales larger than the mesoscales. Time-series of $MP^{Cg}$ from all three stress formulations are to leading order similar and exhibit the same seasonal trends, peaking in the local winter. This is simply an indication that stronger winter winds deposit more energy, regardless of the stress used. Differences between the three formulations are of order $\approx 10\%$ or less. For example, on a global average, we see that $\boldsymbol{\tau}_a$ deposits 10% more energy into the large-scales compared to $\boldsymbol{\tau}_{qs}$, whereas $\boldsymbol{\tau}_r$ deposits a reasonably accurate amount of energy at those large-scale, consistent with our observations from Fig. 6.

The time-series of $MP^{Cg}$ in Fig. 8B, C, E, F also show that WBCs are strongly forced by winds at large-scales. In the case of the Gulf Stream and Kuroshio, this forcing decreases to zero in the summer and early autumn, even becoming slightly negative in the Kuroshio.

In summary, we find that all three wind stress formulations do a reasonably accurate (within 10%) job at driving the ocean circulation at length-scales larger than the mesoscales. They also seem to capture regional and seasonal variations well. On the other hand, the three wind stress formulations show stark differences in how they drive the mesoscales. Our benchmark QuikSCAT stress, $\boldsymbol{\tau}_{qs}$, leads to mesoscales being killed, which exhibits a seasonal winter peak. In contrast, NCEP absolute stress, $\boldsymbol{\tau}_a$, does negligible (albeit positive) work on the mesoscales and without a clear seasonality, while NCEP relative stress, $\boldsymbol{\tau}_r$, leads to eddy killing that is artificially inflated at $\approx 4\times$ the levels seen from $\boldsymbol{\tau}_{qs}$. In section 6, we shall offer an explanation for these discrepancies in mesoscale wind work among the three wind stresses. In section 7, we offer a simple reformulation of $\boldsymbol{\tau}_r$ that removes its artifacts.

## 6 Explaining the Scale Coupling Physics

In this section, we shall discuss an analytical expression (see supplementary section in Rai et al. (2021)) that gives us insight into the physics of wind work as quantified by $EP^{Cg}$. Our expression allows us to determine a necessary criterion for eddy-killing to operate at any length-scale, which explains why NCEP relative wind stress, $\boldsymbol{\tau}_r$, yields exaggerated eddy killing at the mesoscales as we showed above. It will also guide us to propose a fix in the following section 7.

### 6.1 Analytical Expression

Starting from the formulation of relative wind stress in eq. (3), wind work on the ocean is

$$\boldsymbol{\tau}_r \cdot \mathbf{u}_o = \underbrace{\rho_{air}\, C_d |\mathbf{u}_a - \mathbf{u}_o| (\mathbf{u}_a - \mathbf{u}_o)}_{\boldsymbol{\tau}_r} . \mathbf{u}_o \tag{20}$$

Following Eyink (2005), wind work on scales $< \ell$, $EP^{Cg}$ in eq. (13), can be rewritten via an exact identity as (see section 2.4 in Aluie (2017) for details)

$$EP^{Cg}_\ell = \overline{\boldsymbol{\tau}_r \cdot \mathbf{u}_o} - \overline{\boldsymbol{\tau}}_r \cdot \overline{\mathbf{u}_o} = \{\delta\boldsymbol{\tau}_r \cdot \delta\mathbf{u}_o\}_\ell - \{\delta\boldsymbol{\tau}_r\}_\ell \cdot \{\delta\mathbf{u}_o\}_\ell \ , \tag{21}$$

where $\delta f(\mathbf{x};\mathbf{r}) = f(\mathbf{x}+\mathbf{r}) - f(\mathbf{x})$ are increments and $\{\dots\}_\ell \equiv \int dArea\ G_\ell(\mathbf{r})(\dots)$ is an area average over separations $|\mathbf{r}| < \ell$ around location $\mathbf{x}$, weighted by coarse-graining kernel $G_\ell(\mathbf{r})$. Relation (21), which is exact, can be approximated as (see section 2.4 in Aluie (2017))

$$EP^{Cg}_\ell = \{\delta\boldsymbol{\tau}_r \cdot \delta\mathbf{u}_o\}_\ell - \{\delta\boldsymbol{\tau}_r\}_\ell \cdot \{\delta\mathbf{u}_o\}_\ell \approx [\boldsymbol{\tau}_r]'_\ell \cdot [\mathbf{u}_o]'_\ell \tag{22}$$

where, the operation $[\dots]'_\ell$ is defined as the contribution from scales smaller than $\ell$ such that $[f(\mathbf{x})]'_\ell = f(\mathbf{x}) - \overline{f}_\ell(\mathbf{x})$. This is not to be confused with the fluctuating component from Reynolds averaging in eq. (7), which is denoted with just a prime ($'$).

Therefore, wind work on scales $< \ell$ at any geographic location can be written as

$$\begin{aligned} EP^{Cg}_\ell &\approx [\boldsymbol{\tau}_r]'_\ell \cdot [\mathbf{u}_o]'_\ell \\ &= \rho_{air}\, C_d \left[\, |\mathbf{u}_a - \mathbf{u}_o| \, (\mathbf{u}_a - \mathbf{u}_o)\right]'_\ell \cdot [\mathbf{u}_o]'_\ell \ . \end{aligned} \tag{23}$$

We can further simplify this expression, first by noting that wind speed is much larger than the ocean current, $|\mathbf{u}_a| \gg |\mathbf{u}_o|$, typically by $O(10)$ to $O(100)$, such that $|\mathbf{u}_a - \mathbf{u}_o| \approx |\mathbf{u}_a|$. Our expression becomes

$$EP^{Cg}_\ell \approx \rho_{air}\, C_d \left[\, |\mathbf{u}_a| \, (\mathbf{u}_a - \mathbf{u}_o)\right]'_\ell \cdot [\mathbf{u}_o]'_\ell \ . \tag{24}$$

Moreover, wind speed is dominated by scales $> O(10^3)$ km (Nastrom et al., 1984; Burgess et al., 2013), implying a separation of scales between those of wind and ocean velocities. This justifies

$$\left[\, |\mathbf{u}_a| \, (\mathbf{u}_a - \mathbf{u}_o)\right]'_\ell \approx |\mathbf{u}_a| [\mathbf{u}_a - \mathbf{u}_o]'_\ell \ , \tag{25}$$

which essentially treats the wind speed factor $|\mathbf{u}_a|$ as spatially constant at oceanic scales $\ell < 10^3$ km.

This leads to our final expression for wind work on scales $< \ell$ at any geographically local position,

$$\begin{aligned} EP^{Cg}_\ell &\approx \rho_{air}\, C_d |\mathbf{u}_a| [\mathbf{u}_a - \mathbf{u}_o]'_\ell \cdot [\mathbf{u}_o]'_\ell \\ &= \rho_{air}\, C_d |\mathbf{u}_a| \Big( [\mathbf{u}_a]'_\ell \cdot [\mathbf{u}_o]'_\ell \underbrace{- [\mathbf{u}_o]'_\ell \cdot [\mathbf{u}_o]'_\ell}_{\text{negative}} \Big). \end{aligned} \tag{26}$$

The first term in the final expression in eq. (26) is the work done by small-scale winds ($< \ell$) on small-scale ocean currents. The second term in eq. (26) is negative semi-definite. It is the underlying cause of eddy killing and accounts for the negative values of $EP^{Cg}$. Note that both of these scale processes, as well as $EP^{Cg}_\ell$ in eq. (26), are local in $\mathbf{x}$, which allows us to probe their behavior geographically and not just in a spatially averaged manner.

From eq. (26), we derive the condition for eddy-killing to occur:

$$[\mathbf{u}_a]'_\ell \cdot [\mathbf{u}_o]'_\ell - [\mathbf{u}_o]'_\ell \cdot [\mathbf{u}_o]'_\ell < 0 \qquad \text{(eddy-killing criterion)}. \tag{27}$$

Eq. (27) highlights the role of small-scale winds, $[\mathbf{u}_a]'_\ell$. If $[\mathbf{u}_a]'_\ell$ is of a significant magnitude and aligned with small-scale ocean currents, $[\mathbf{u}_o]'_\ell$, then wind stress energizes eddies rather than kill them, and we have $EP^{Cg}_\ell > 0$. Wind speed, $|\mathbf{u}_a|$ in eq. (26), acts as an amplification factor for either eddy-killing or eddy-energization. Therefore, the presence or absence of small-scale winds $[\mathbf{u}_a]'_\ell$, even if weak, can have a disproportionate effect (because $|\mathbf{u}_a|$ is large) on the wind work done on the small-scale oceanic currents $< \ell$. In the next subsection, we further elaborate on these issues using illustrative numerical examples of eddy-killing and eddy-energization.

These considerations based on eq. (26) provide an explanation for the exaggerated eddy-killing, $EP^{Cg}_r \approx 4 \times EP^{Cg}_{qs}$, which we observed above when using relative wind stress, $\boldsymbol{\tau}_r$. Since NCEP winds are at a coarser resolution (gridded at 2°) than the ocean currents (gridded at 1/4°), if $\ell$ in eq. (26) is taken to be smaller than the resolution scale of NCEP, we have $[\mathbf{u}_a]'_\ell = 0$. Therefore, a coarser wind resolution artificially sets $[\mathbf{u}_a]'_\ell \cdot [\mathbf{u}_o]'_\ell = 0$ in eq. (26), leaving only the negative term arising from the small-scale ocean currents. It is the mismatch in resolution between $\mathbf{u}_a$ and $\mathbf{u}_o$ that is the root of the problem.

In comparison, $EP^{Cg}_{qs}$ does not suffer from these artifacts since it is based on QuikSCAT wind stress, $\boldsymbol{\tau}_{qs}$, from which wind velocity $\mathbf{u}_{qs}$ is inherently relative to the oceanic flow (Cornillon & Park, 2001; Kelly et al., 2001) as we discussed in section 4. This necessarily implies that $\mathbf{u}_a$ and $\mathbf{u}_o$ within the stress formulation are at the same resolution. In other words, when using wind stress from scatterometry, the factor $[\mathbf{u}_a - \mathbf{u}_o]'_\ell$ in the first expression of eq. (26) is replaced by $[\mathbf{u}_a - \mathbf{u}_o]'_\ell = [\mathbf{u}_{qs}]'_\ell$, precluding artifacts from resolution mismatch that appear in the NCEP relative stress. Since $EP^{Cg}_{qs}$ is also negative but with a magnitude smaller than that of $EP^{Cg}_r$, we can infer that on average

$$[\mathbf{u}_o]'_\ell \cdot [\mathbf{u}_o]'_\ell > [\mathbf{u}_a]'_\ell \cdot [\mathbf{u}_o]'_\ell > 0 \ . \tag{28}$$

Eq. (28) implies that small-scale winds $[\mathbf{u}_a]'_\ell$ tend to be aligned, on average, with small-scale currents $[\mathbf{u}_o]'_\ell$ but are not sufficiently strong to render $[\mathbf{u}_a]'_\ell \cdot [\mathbf{u}_o]'_\ell - [\mathbf{u}_o]'_\ell \cdot [\mathbf{u}_o]'_\ell$, and thereby $EP^{Cg}_{qs}$ from eq. (26), positive. The tendency for small-scale winds and currents to be aligned may be due to the so-called "re-energization" mechanism identified by Renault, Molemaker, McWilliams, et al. (2016), in which winds mechanically adjust to the ocean observed surface state. What we are highlighting here, based on eq. (26), is that such adjustment is not even possible at the scale of oceanic eddies if the atmosphere's resolution is coarser than the ocean's even in coupled atmosphere-ocean models. Such resolution mismatch can lead to significant artifacts in the wind forcing of ocean mesoscales as we showed from a comparison of $EP^{Cg}_r$ to $EP^{Cg}_{qs}$ above.

If wind stress is formulated using absolute winds as in eq. (2), then eq. (26) becomes

$$EP^{Cg}_a \approx \rho_{air} C_d |\mathbf{u}_a| [\mathbf{u}_a]'_\ell \cdot [\mathbf{u}_o]'_\ell \ . \tag{29}$$

This shows that when forcing the ocean with $\boldsymbol{\tau}_a$, wind work on the eddies, $[\mathbf{u}_o]'_\ell$, only depends on their alignment with small-scale winds, $[\mathbf{u}_a]'_\ell$. The negative term in eq. (26) is absent from eq. (29). If small-scale winds are absent, $[\mathbf{u}_a]'_\ell = 0$, as in the case of the NCEP winds at scales $< 200$ km due to the coarse resolution of the dataset, then $\boldsymbol{\tau}_a$ can cause neither eddy-killing nor eddy-energization at scales $\ell < 200$ km, and we get $EP^{Cg}_a \approx 0$. This can be seen from Fig. 6A, where the orange plot of $EP^{Cg}_a(\ell)$ is negligible at scales smaller than 200 km and only increases significantly at larger scales. The same behavior holds in all panels of Fig. 6, representing all regions we analyzed.

### 6.2 Demonstrating Eddy Killing with Toy Examples

Fig. 9 illustrates our expression (26) under various air-sea configurations. They show the conditions under which the eddy-killing criterion in eq. (27) is satisfied and those under which eddies are energized by wind.

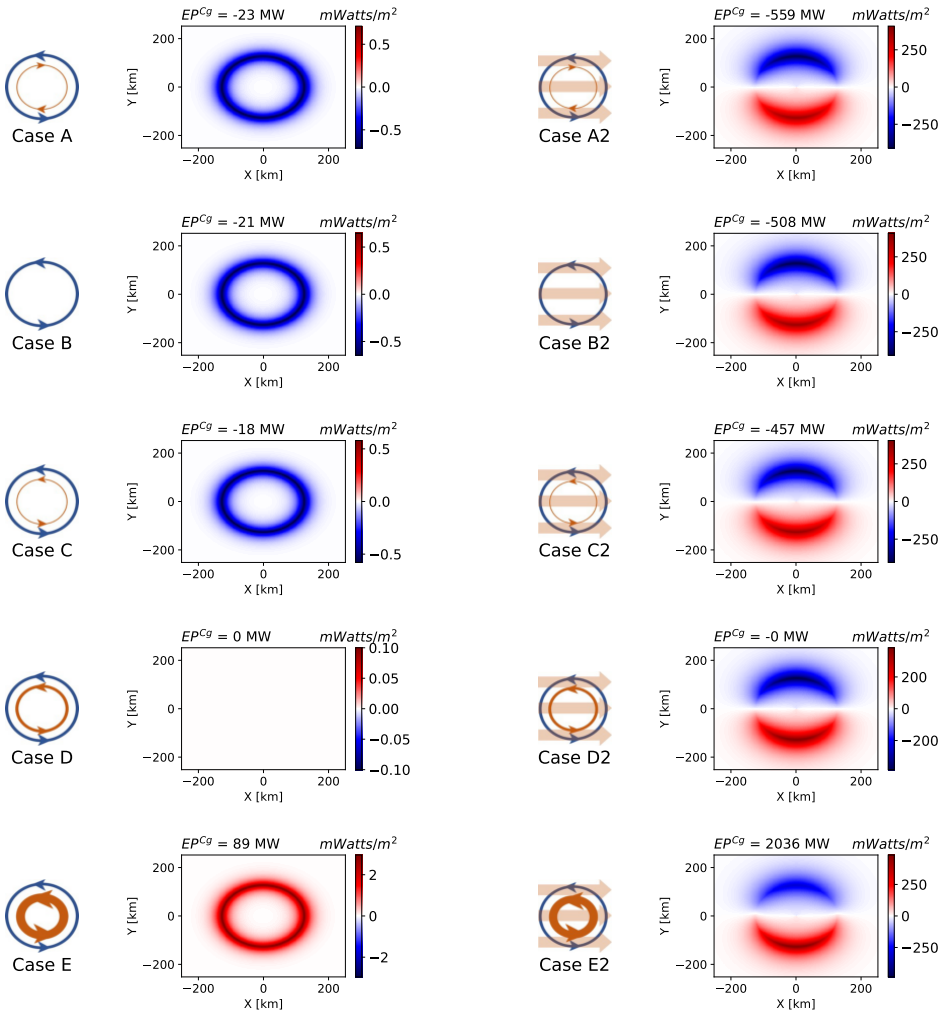


Figure 9: Cases illustrating eddy-killing and eddy-energization, which highlight the disproportionate role small-scale winds have on air-sea coupling. Each panel shows a schematic (left) of the air-sea state along with a numerical realization (right). In the schematics, a blue circular flow represents an oceanic eddy, $[\mathbf{u}_o]'_\ell$. The brown circular flow represents a wind eddy, $[\mathbf{u}_a]'_\ell$, that is of the same scale as and spatially co-located with the oceanic eddy. The thickness of the wind eddy represents its strength relative to the oceanic eddy. Left-row panels are identical to right-row, but lack a uniform background (large-scale) wind, which is represented by three thick brown parallel arrows. In the numerical realizations, red (blue) represents positive (negative) wind work. The domain-integrated wind work is reported at the top of the respective numerical realization. In accord with the eddy killing criterion (eq. (27)), cases D, D2, E and E2 lack eddy killing, unlike rest of the cases. The standard schematic of eddy killing in Fig. 1 is case B2 is only a special case of several other possible (and more probable) states leading to eddy-killing. Though the schematics here show closed circular flows to represent eddies, more general configurations of wind and ocean currents can have an equivalent effect without requiring closed circular paths.

The standard schematic of eddy killing in figure 1 is shown as case B2 in Fig. 9. In Fig. 9, each panel includes a schematic on the left of wind velocity (brown) and the oceanic eddy (blue). On the right of each panel, we also show an evaluation of wind work on the

oceanic eddy, $EP^{Cg}$ in eq. (21), using a numerical realization of the corresponding air-sea state.

In all schematics of Fig. 9, the blue circular flow represents an oceanic eddy, $[\mathbf{u}_o]'_\ell$. The brown circular flow represents a wind eddy, $[\mathbf{u}_a]'_\ell$, that is of the same scale as and spatially co-located with the oceanic eddy. The thickness of the wind eddy represents its strength relative to the oceanic eddy. All left panels in Fig. 9 are identical to those on their right, but lack a uniform background (large-scale) wind, which is represented by three thick brown parallel arrows.

For each case in Fig. 9, we construct corresponding numerical data as we shall now describe. In a doubly periodic domain of 500 km in extent, we construct an ocean-eddy that is a circular current of diameter $\approx$ 300 km. This is done by generating sea-surface height (SSH) with a guassian profile and an e-folding length-scale of 40 km and maximum height of $\approx 0.25$ m. The associated geostrophic ocean current in the f-plane is calculated from the SSH using a constant $f = 0.7\times10^{-4}$ sec$^{-1}$. This yields an ocean current with peak speed of $\approx 0.4$ m/ sec. The same velocity field is then used for constructing the wind eddy but with a modified speed factor corresponding to the schematic. The weaker atmospheric eddy is $0.1\times$ the ocean eddy's speed. The stronger wind eddy has $5\times$ the speed of the ocean eddy. The large-scale uniform winds have a constant eastwards speed of 20 m/sec. Wind stress is then formulated from relative wind velocity using eqs. (16) and (17) from section 5.1.

Eddy-killing occurs in the top six panels of Fig. 9, all of which satisfy the criterion in eq. (27). Of the remaining four cases, two are eddy-energizing (E and E2) and two have net zero wind work (D and D2).

Among the eddy-killing cases, we can see that those with a background large-scale wind (A2, B2, C2) experience higher levels of eddy-killing compared to the counterparts without a large-scale wind on the left of Fig. 9. The same effect can also be seen in the eddy-energizing cases E and E2. This highlights the amplifying role of background winds via the factor $|\mathbf{u}_a|$ in eq. (21), which we discussed in the previous subsection.

Case B shows how the atmosphere can kill ocean eddies even in the complete absence of winds, either small-scale wind eddies or large-scale background winds. In this case, we have $\mathbf{u}_a = 0$, including $[\mathbf{u}_a]'_\ell = 0$, and yet $EP^{Cg} < 0$ in eq. (21). This can be seen analytically starting from eq. (21) and following steps similar to those we used to arrive at eq. (26), except for the approximation $|\mathbf{u}_a - \mathbf{u}_o| \approx |\mathbf{u}_a|$ now replaced with $|\mathbf{u}_a - \mathbf{u}_o| = |\mathbf{u}_o|$ to get

$$\begin{aligned} EP^{Cg}_\ell &\approx \rho_{air}\, C_d |\mathbf{u}_o| [\mathbf{u}_a - \mathbf{u}_o]'_\ell \cdot [\mathbf{u}_o]'_\ell \\ &= \rho_{air}\, C_d |\mathbf{u}_o| \Big( 0 - [\mathbf{u}_o]'_\ell \cdot [\mathbf{u}_o]'_\ell \Big) \end{aligned} \tag{30}$$

for case B in Fig. 9. In this configuration, the atmosphere is merely acting as a solid upper boundary for the ocean, exerting a drag comparable to that at the ocean bottom (Dewar & Flierl, 1987). Case B2 is similar but more realistic in having large-scale winds, which amplify the eddy-killing seen in case B. For case B2, the analytical expression in eq. (26) with $[\mathbf{u}_a]'_\ell = 0$ describes the physics.

Cases B and B2 underscore how spurious eddy-killing can occur in general circulation models if the atmospheric resolution is coarser than that of the ocean. If the atmosphere is unable to accommodate motions on scales similar to those present in the ocean due to its coarse grid, then small-scale oceanic motions (e.g. eddies) will experience an artificial drag due to the atmosphere's inability to flow at those small-scales. Such spurious eddy-killing due to resolution mismatch can be severe as we showed in the case of NCEP winds in section 5.4, which exaggerates eddy-killing by a factor of $\approx 4$.

Cases A & A2 and C & C2 in Fig. 9 show a variation on cases B & B2 by including a weak wind eddy. In cases A & A2, where the wind eddy is counter-rotating relative to the ocean eddy ($[\mathbf{u}_a]'_\ell \cdot [\mathbf{u}_o]'_\ell < 0$ in eq. (26)), it increases the intensity of eddy-killing. In cases

C & C2, where the wind eddy is co-rotating relative to the ocean eddy ($[\mathbf{u}_a]'_\ell \cdot [\mathbf{u}_o]'_\ell > 0$ in eq. (26)), it decreases the intensity of eddy-killing. All of these cases can be manifested in the real ocean in the presence of thermal feedback onto the atmosphere. Due to instability of the atmospheric boundary layer, wind is faster over warmer surface water than the colder water at SST fronts (e.g. O'Neill, 2012; Tokinaga et al., 2005). SST anomalies are not usually concentric with SSH anomalies in warm/cold core eddies (e.g. Hausmann & Czaja, 2012; Liu et al., 2020). Feedback from SST anamolies onto the wind speed can give rise to a wind velocity gradient that can be equivalent to a wind eddy that is either co-rotating or counter-rotating relative to the ocean eddy. Moreover, the mechanical feedback from the ocean eddy onto the atmosphere can give rise to a co-rotating atmospheric eddy as in cases C & C2, thereby reducing the intensity of eddy-killing. This is the re-energization process described in Renault, Molemaker, McWilliams, et al. (2016) and a probable reason why $EP_{qs}^{Cg}$ measured from QuikSCAT winds yields intermediate levels of eddy-killing we found in section 5.4.

Cases D & D2 in Fig. 9 also include a wind eddy, which has a velocity matching that of the ocean eddy such that $[\mathbf{u}_a]'_\ell \cdot [\mathbf{u}_o]'_\ell - [\mathbf{u}_o]'_\ell \cdot [\mathbf{u}_o]'_\ell = 0$ in eq. (26). In these configurations, there is a net zero wind work done despite the presence of background winds in case D2.

Cases E & E2 in Fig. 9 show that it is even possible for wind work to be positive, *i.e.* have eddy-energization rather than eddy-killing, if the wind eddy is co-rotating with the ocean eddy and is faster than it ($[\mathbf{u}_a]'_\ell \cdot [\mathbf{u}_o]'_\ell - [\mathbf{u}_o]'_\ell \cdot [\mathbf{u}_o]'_\ell > 0$ in eq. (26)). These cases underscore that the main determinant of the presence of eddy-killing is the criterion in eq. (27) and not the background winds, which exist in case E2.

In summary, Fig. 9 shows how the mechanical coupling between the atmosphere and the oceanic mesoscales can be significantly distorted if the atmospheric motions at those same scales are misrepresented in a model. Even though the dominant atmospheric motions are at length-scales larger than $O(10^3)$ km, winds at scales $O(10^2)$ km can have a disproportionate effect on the dynamics of mesoscale ocean eddies. The effect of small-scale winds is captured in eq. (26) and illustrated in Fig. 9. In addition to their mechanical feedback onto the atmosphere, oceanic eddies also have core temperatures different from the background, which leads to thermal feedbacks. Both mechanical and thermal feedbacks onto winds are at the length-scale of the oceanic eddies and can excite small-scale winds, which can alter eddy killing. We have shown how an atmosphere that is at a coarser resolution than the ocean will lead to exaggerated eddy-killing. In the following section, we propose a fix by a simple reformulation of the wind stress.

## 7 Implications to Modeling

Our study has practical relevance to forcing ocean models. Consistent with previous work (e.g., Duhaut & Straub, 2006; Renault, Molemaker, McWilliams, et al., 2016), we have shown that forcing an ocean with absolute wind stress that is only a function of wind velocity, such as NCEP $\boldsymbol{\tau}_a$ we analyzed above, overestimates overall wind work, especially at small scales because of a lack of eddy-killing. Attempting to remedy this artifact by using stress that is a function of relative wind velocity, such as $\boldsymbol{\tau}_r$ we analyzed above, underestimates wind work because of a significant exaggeration of eddy-killing. This arises from resolution mismatch between the atmospheric velocity and the ocean surface current. Using coarser atmospheric grids in coupled atmosphere-ocean GCMs is the norm. For example, the atmospheric resolution relative to the ocean's is 4× coarser in GFDL's CM4.0 model (Held et al., 2019), 5× coarser in the Met Office Hadley Centre's HadGEM3-GC31-HH model (Roberts, 2018), and 10× coarser in their HadGEM3-GC31-LM model (Roberts, 2017). All three example models contribute to CMIP6 and have an eddy-permitting ocean with nominal grid resolutions of 25 km, 10 km, and 25 km, respectively.

These models suffer from a systematic bias due to an atmosphere-ocean resolution mismatch based on our theoretical and data analysis above. As we have discussed, the bias from exaggerated eddy-killing arises when oceanic eddies are unable to generate atmospheric motions at the same scale. These biases are not distributed uniformly but are concentrated in dynamic regions such as WBCs where most of the spurious eddy-killing occurs (compare Fig. 3F to Fig. 3B).

To see how an atmosphere-ocean resolution mismatch biases a model toward exaggerated eddy-killing, consider the expression in eq. (26), which quantifies wind work at all scales smaller than $\ell$ resolved in the ocean component of a model. If the atmospheric grid resolution is $\Delta$ and the oceanic grid resolution is $\delta < \Delta$, then setting $\ell = \Delta$ in eq. (26) gives wind work at all resolved oceanic scales smaller than $\Delta$,

$$EP^{Cg}_{\Delta} \;=\; \rho_{air}\, C_d |\mathbf{u}_a| \Big( \underbrace{[\mathbf{u}_a]'_\Delta \cdot [\mathbf{u}_o]'_\Delta}_{=0} - [\mathbf{u}_o]'_\Delta \cdot [\mathbf{u}_o]'_\Delta \Big) = -\rho_{air}\, C_d |\mathbf{u}_a| [\mathbf{u}_o]'_\Delta \cdot [\mathbf{u}_o]'_\Delta \;. \tag{31}$$

The first term in the parentheses vanishes because the atmospheric grid cannot allow motions at scales smaller than $\Delta$, *i.e.* $[\mathbf{u}_a]'_\Delta = 0$. This biases wind work to being artificially negative in the last expression in eq. (31), which is negative semi-definite. The situation is best illustrated by case B2 in Fig. 9. In more realistic settings, it can be seen from evaluating wind work using the NCEP relative stress, $\boldsymbol{\tau}_r$, which yields $EP^{Cg}_r \approx -200$ GW that is four times the eddy-killing value found from the more accurate QuikSCAT stress ($\boldsymbol{\tau}_{qs}$). NCEP winds are approximately 8× coarser than the ocean currents from altimetry.

If the atmosphere has sufficient grid resolution, it can respond to the oceanic eddies by generating co-rotating eddies of the same size, such that $[\mathbf{u}_a]'_\Delta \cdot [\mathbf{u}_o]'_\Delta > 0$. This situation, illustrated by case C2 in Fig. 9, reduces the intensity of eddy-killing. Indeed, having the more accurate QuikSCAT stress $\boldsymbol{\tau}_{qs}$ yielding $EP^{Cg}_{qs}$ that is less negative than $EP^{Cg}_r$ is a concomitant indication that atmospheric motions at scales smaller than 200 km tend to be aligned with oceanic motions at those scales on average.

It is important to bear in mind that our analysis is diagnostic and does not take into account feedbacks. For example, consider a benchmark coupled atmosphere-ocean model (M1) with equal atmosphere-ocean grid resolution and another test model (M2) with resolution mismatch. It is very likely that forcing the ocean with relative wind stress $\boldsymbol{\tau}_r$, which is biased toward dampening the mesoscales if the resolution is mismatched, would lead to a weakened eddy field in M2. Therefore, eddy-killing may be weaker (not exaggerated) in M2 relative to M1 due to the feedback, which yields a weaker eddy field. The negative term in eq. (26) shows that eddy-killing is proportional to the energy residing in the eddies.

For example, in our previous work (see Supplementary Materials in (Rai et al., 2021)) we analyzed the spectral energy disribution in a global coupled 0.1° ocean from the Community Earth System Model (CESM) (R. J. Small et al., 2014). We found that compared to AVISO, CESM has systematically weaker mesoscales and a spectral peak that is shifted toward smaller scales. We had speculated in Rai et al. (2021) that one possible cause for such bias may be a weaker inverse cascade in CESM, which at a 0.1° ocean resolution does not resolve the sub-mesoscales. Another possible cause, based on our discussion here, is spurious spurious eddy killing from resolution mismatch since the CESM atmosphere is 2.5× coarser than the ocean[4].

### 7.1 Wind stress recipe to fix exaggerated eddy-killing

Having identified the root cause of the systematic bias toward exaggerated eddy-killing as being due to atmosphere-ocean resolution mismatch, we can now offer a simple reformu-

[4] Despite weaker mesoscales, Rai et al. (2021) found that CESM has slightly stronger eddy-killing of −55 GW due to artificially strong winds (R. J. Small et al., 2014).

lation of the wind stress to alleviate this bias. Since the atmospheric timescales are much faster than the oceanic timescales, increasing the atmospheric resolution to match that of the ocean can be computationally prohibitive. Indeed, almost all coupled GCMs use an atmospheric grid that is at least a factor of 2 coarser than the ocean's and in some instances is 10× coarser (e.g. Roberts (2017)).

The idea is to define wind stress using wind velocity not relative to the ocean velocity, $\mathbf{u}_a - \mathbf{u}_o$, as in $\boldsymbol{\tau}_r$ in eq. (3) or eq. (16), but relative to a coarsened ocean velocity,

$$\mathbf{u}_{r2} = \mathbf{u}_a - \overline{(\mathbf{u}_o)}_\Delta \ . \tag{32}$$

Here, the atmospheric grid resolution is $\Delta$ and the oceanic grid resolution is assumed to be $\delta < \Delta$. The simple reformulation of the bulk stress we propose (see Table 1) is

$$\boldsymbol{\tau}_{r2} = \mathbf{u}_{r2}\, F(u_{r2}) \ , \tag{33}$$

where $F(u_{r2})$ is given by eq. (17). Eq. (33) essentially matches the surface ocean currents' resolution to that of the atmosphere when formulating wind stress.

To see why the stress formulation in eq. (33) fixes the bias, consider wind work by $\boldsymbol{\tau}_{r2}$ on all scales $< \ell$,

$$EP_{r2}^{Cg}(\ell) = \overline{\boldsymbol{\tau}_{r2}\cdot\mathbf{u}_o} - \overline{\boldsymbol{\tau}}_{r2}\cdot\overline{\mathbf{u}}_o \ . \tag{34}$$

This is the same as $EP^{Cg}$ in eq. (13) but using $\boldsymbol{\tau}_{r2}$ as the wind stress. Note that the coarsened ocean surface velocity, $\overline{(\mathbf{u}_o)}_\Delta$, only enters via the prognostic wind stress variable $\boldsymbol{\tau}_{r2}$ in eq. (33). When diagnosing wind work in eq. (34), $\mathbf{u}_o$ is the (un-coarsened) ocean surface velocity at its native ocean grid resolution. Repeating the reasoning leading to eq. (31) but using the reformulated stress $\boldsymbol{\tau}_{r2}$ in eq. (13), we find that wind work at all resolved oceanic scales smaller than $\Delta$ is

$$EP_{r2}^{Cg}(\Delta) = \rho_{air}\, C_d |\mathbf{u}_a| \Big( [\mathbf{u}_a]'_\Delta - [\overline{(\mathbf{u}_o)}_\Delta]'_\Delta \Big) \cdot [\mathbf{u}_o]'_\Delta \tag{35a}$$

$$= \rho_{air}\, C_d |\mathbf{u}_a| \Big( \underbrace{[\mathbf{u}_a]'_\Delta \cdot [\mathbf{u}_o]'_\Delta}_{=0} - \underbrace{[\overline{(\mathbf{u}_o)}_\Delta]'_\Delta \cdot [\mathbf{u}_o]'_\Delta}_{\text{small}} \Big) \ . \tag{35b}$$

The second term in the parentheses is small in magnitude because of the $[\overline{(\mathbf{u}_o)}_\Delta]'_\Delta$ factor. This is a simple consequence of formulating $\boldsymbol{\tau}_{r2}$ using the coarsened ocean velocity $\overline{(\mathbf{u}_o)}_\Delta$, which has variations at scales $< \Delta$ greatly attenuated but not completely removed. As mentioned in section 3, Reynolds averaging or truncation of the Fourier series are projection operators, while a general coarsening of a field, such as by averaging adjacent grid cells, does not have to satisfy $\overline{(\overline{\mathbf{u}}_\Delta)}_\Delta = \overline{\mathbf{u}}_\Delta$. Therefore, $|[\overline{(\mathbf{u}_o)}_\Delta]'_\Delta|$ is smaller than $|[\mathbf{u}_o]'_\Delta|$ but is not generally zero.

Unlike an ocean forced by relative wind stress, $\boldsymbol{\tau}_r$, which leads to exaggerated eddy-killing if atmosphere-ocean resolution is mismatched, eq. (35b) shows that $\boldsymbol{\tau}_{r2}$ does significantly less eddy-killing on scales smaller than $\Delta$, the atmospheric resolution. One can regard our fix as a way to account for the alignment that would have been present between $[\mathbf{u}_a]'_\Delta$ with $[\mathbf{u}_o]'_\Delta$ had the atmosphere been at the higher ocean resolution. Such alignment would reduce the magnitude of $[\mathbf{u}_a]'_\Delta - [\mathbf{u}_o]'_\Delta$ in expression (35a). However, with $[\mathbf{u}_a]'_\Delta = 0$ due to insufficient resolution, a convenient way to account for such missing alignmnet is to attenuate $[\mathbf{u}_o]'_\Delta$ by replacing it with $[\overline{(\mathbf{u}_o)}_\Delta]'_\Delta$ in eq. (35a). The simplicity of $\boldsymbol{\tau}_{r2}$ and its lack of any free parameters (see eq. (33)) makes it especially appealing. As we shall now discuss, the wind work $EP_{r2}^{Cg}$ done by $\boldsymbol{\tau}_{r2}$ is remarkably accurate when compared to our benchmark $EP_{qs}^{Cg}$ from QuikSCAT stress, $\boldsymbol{\tau}_{qs}$.

To evaluate the stress formulation $\boldsymbol{\tau}_{r2}$ in eq. (33), we use NCEP winds $\mathbf{u}_a$ which have $2^\circ \times 2^\circ$ grid resolution (see Table 1) and the ocean surface velocity from altimetry, $\mathbf{u}_o$, which is on a $0.25^\circ \times 0.25^\circ$ grid. We filter the latter by performing a simple $2^\circ \times 2^\circ$ box averaging

to better match the NCEP winds resolution, yielding a coarsened[5] ocean velocity $\widetilde{\mathbf{u}_o}$. From eq. (13), we then evaluate the wind work $EP_{r2}^{Cg}(\ell)$ at all scales $< \ell$ using $\boldsymbol{\tau}_{r2}$ for the stress and the uncoarsened ocean velocity $\mathbf{u}_o$.

Plots of $EP_{r2}^{Cg}$ as a function of $\ell$ in different regions are shown in Fig. 6. All panels show a remarkable improvement in $EP_{r2}^{Cg}$ (maroon plots) over $EP_{r}^{Cg}$ (green) when compared to our benchmark $EP_{qs}^{Cg}$ (blue). The magnitude of eddy-killing inferred from the minimum value of the $EP_{r2}^{Cg}$ is almost the same as that from $EP_{qs}^{Cg}$ in each of the regions. The equator region yields the poorest result, which may be due to using altimetery derived geostrophic velocities, which are not as accurate in that region, and an absence of eddy-killing derived from QuikSCAT. The minima of $EP_{r2}^{Cg}$ are systematically at slightly larger scales than those of $EP_{qs}^{Cg}$, but this is due to using coarse NCEP winds. The latter can only drive the ocean at the length-scales it resolves, via the term $[\mathbf{u}_a]'_\ell \boldsymbol{\cdot} [\mathbf{u}_o]'_\ell$ in eq. (26). Indeed, plots of $EP_{r}^{Cg}$ in Fig. 6 have minima at the same scales as $EP_{r2}^{Cg}$.

Times series of $EP_{r2}^{Cg}$ in Fig. 7 show that the reformulated stress $\boldsymbol{\tau}_{r2}$ does well not just in a time-averaged sense, but at all times and in all regions. In all panels of Fig. 7, we see that plots of $EP_{r2}^{Cg}$ (maroon) are much closer to $EP_{qs}^{Cg}$ (blue) than wind work $EP_{r}^{Cg}$ (green) done by the standard relative wind stress formulation $\boldsymbol{\tau}_r$. Times series of $MP_{r2}^{Cg}$ in Fig. 8 shows that the reformulated stress only alters the forcing of scales smaller than $\approx 400$ km. In all panels of Fig. 8, we see that plots of $MP_{r2}^{Cg}$ (maroon) are almost indistinguishable from $MP_{r}^{Cg}$ (green), which quantifies wind work done by $\boldsymbol{\tau}_r$ on all scales larger than $\approx 400$ km. This is unsurprising since the reformulation $\boldsymbol{\tau}_{r2}$ coarsens the ocean velocity only at the smallest scales, close to those of the atmospheric grid.

### 7.2 Ocean-only Models

So far, we have discussed the benefits of reformulated wind stress $\boldsymbol{\tau}_{r2}$ (eq. (33)) in the context of coupled atmosphere-ocean models. Ocean-only models, which rely on a prescribed wind stress, present a greater challenge in the proper representation of eddy-killing and has been the focus of several studies (Renault, Molemaker, Gula, et al., 2016; Renault et al., 2020; Lemarié et al., 2021). For example the state-of-the-art LLC4320 ocean-only simulation has a nominal resolution of $1/48^\circ$ and is forced by relative winds from ECMWF analysis on a $0.14^\circ$ grid (Menemenlis et al., n.d.). Therefore, the atmosphere in that model $\approx 7\times$ coarser than the ocean, guaranteeing a systematic bias toward over-damping oceanic scales smaller than the atmospheric resolution based on our results above.

Complicating matters further, in ocean-only models, the atmosphere cannot respond to the oceanic mesoscales by definition, regardless of the atmospheric grid resolution. Unlike large-scale currents, the oceanic mesoscales are chaotic and unpredictable. Therefore, it is not reasonable to expect the prescribed small-scale atmospheric motions to align with the oceanic mesoscales deterministically.

For ocean-only simulations, Renault et al. (2020) proposes modifications to the wind-ocean coupling coefficients to account for the possibility of wind re-energization by mesoscale eddies. Lemarié et al. (2021) proposes the introduction of a Marine Atmospheric Boundary Layer to mediate such coupling, which may include more accurate physics but at a high computational cost. Our expression in eq. (26) for wind work at small-scales offers us a guide for a different approach.

The wind-driven contribution, $[\mathbf{u}_a]'_\ell \boldsymbol{\cdot} [\mathbf{u}_o]'_\ell$ in eq. (26), is expected to be positive in a coupled atmosphere-ocean model. However, in an ocean-only model, the correlation between $[\mathbf{u}_a]'_\ell$ and $[\mathbf{u}_o]'_\ell$ at the mesoscales ($< 400$ km) is unlikely to be significant since the latter are

[5] The lat-long coarsening of $\widetilde{\mathbf{u}_o}$ is not strictly the same as the coarse-grained field $\overline{\mathbf{u}_o}$ in eq. (10) but is easier to implement in a GCM and makes it simpler to match the atmospheric resolution locally.

generated by instabilities. Therefore, it is reasonable to expect that in a space-time average, $[\mathbf{u}_a]'_\ell \cdot [\mathbf{u}_o]'_\ell \approx 0$ at scales smaller than 400 km. In contrast, the contribution $-[\mathbf{u}_o]'_\ell \cdot [\mathbf{u}_o]'_\ell$ to wind work in eq. (26) is always negative and proportional to the energy present at the mesoscales in a model. Therefore, consistent with findings of Renault, Molemaker, McWilliams, et al. (2016), using relative wind stress $\boldsymbol{\tau}_r$ in ocean-only simulations exaggerates eddy-killing for reasons beyond the wind's grid resolution. A slight tweak of $\boldsymbol{\tau}_{r2}$ in eq. (33), by coarsening the ocean velocity not to a level matching the wind's grid resolution as in eq. (32), but to the mesoscales of $\approx 2^\circ \times 2^\circ$ to $4^\circ \times 4^\circ$ may alleviate these shortcomings. Testing this hypothesis is beyond our scope here.

## 8 Limitations of our Analysis

Here, we discuss some of the caveats of our analysis. We also discuss the rationale behind some of the practical choices made in this work.

### 8.1 Data

The QuikSCAT and altimetry datasets we use here are on a $0.25^\circ$ grid but are estimated to have an effective resolution that is $2\times$ to $4\times$ coarser (Mazloff et al., 2014; Desbiolles et al., 2017; Stammer & Cazenave, 2017). This reduction in resolution is compounded by our 7-day running average of the data to allow for global coverage. We believe the eddy killing magnitude will almost certainly increase with the inclusion of scales smaller than the current resolution limit, but that the eddy killing length-scale of $\approx 300$ km is well-resolved within our current analysis and should not change with finer datasets (Rai et al., 2021).

It is also worth mentioning the difficulty in inferring winds from scatterometers under strong wind conditions exceeding $\approx 20$ m/s (Yu & Jin, 2014). Since it is hard to sample these extreme events with a scatterometer and concurrently by other means (in-situ or models), it is challenging to calibrate modeling functions in this regime due to a lack of sufficient reliable benchmarking data (Quilfen et al., 1998; Chelton & Freilich, 2005). Moreover, the measured radar cross-section (or backscatter coefficient) becomes less sensitive to wind under strong wind conditions, increasing the scatterometer's uncertainty in the strong wind regime (Fangohr & Kent, 2012). Fortunately, such strong wind conditions account for a only 2.2% of the global wind field (Yu & Jin, 2014). Yet, we highlight these limitations since correlations (or anti-correlation) between such extreme wind events and oceanic flow, *i.e.* wind work, can still be significant. This is a question for future research.

A salient assumption we have made in our analysis, similar to prior work (Hughes & Wilson, 2008; Scott & Xu, 2009; C. Xu et al., 2016; Renault et al., 2017), is that the (i) sampling of wind stress from QuikSCAT and (ii) the sampling of geostrophic current from altimetry are matched in space and time. A potential mismatch can introduce systematic biases toward smaller values of total wind work and also smaller estimates of eddy killing. However, for such biases to affect our estimates, any time or space mismatch would have to be at (time or length) scales greater than the resolution of our data. Since we use 7-day time-averaged data on a $0.25^\circ$ grid, we believe such biases, if present, are unlikely to be significant.

Another aspect of our analysis worth highlighting is that the QuikSCAT measurement of wind stress $\boldsymbol{\tau}_{qs}$ implicitly involves the full (geostrophic + ageostrophic) ocean velocity interacting with the wind. However, the ocean velocity used in our analysis of wind work represents only the geostrophic flow, $\mathbf{u}_o$, from altimetry, similar to prior work (Hughes & Wilson, 2008; Scott & Xu, 2009; C. Xu et al., 2016; Renault et al., 2017).

Wind work on agesotrophic flow can modify eddy killing which is not accounted for in our study. Two previous studies (Renault, Molemaker, McWilliams, et al., 2016; Renault, Molemaker, Gula, et al., 2016), based on Reynolds averaging, suggest that eddy killing of

the ageostrophic flow may be negligible. Moreover, wind work to the ageostrophic flow is not believed to feed into the general circulation and diapycnal mixing (Wunsch, 1998; Von Storch et al., 2007; Scott & Xu, 2009). In previous work using coarse-graining (see Supplementary Material in (Rai et al., 2021)) to analyze global CESM model output (R. J. Small et al., 2014), we found that the ageostrophic flow is wind-driven and is not subject to eddy killing on average, which is consistent with physical expectations (Renault, Molemaker, McWilliams, et al., 2016; Renault, Molemaker, Gula, et al., 2016). However, upon inspecting regional trends, we found that in strongly eddying regions such as WBCs, the ageostrophic mesoscale flow is also being killed by wind. In contrast, the ageostrophic flow in the rest of the ocean, which includes the Ekman flow, is mostly wind-driven rather than damped. We had hypothesized (Rai et al., 2021) that this may be due to a difference in the formation of ageostrophic mesoscales in energetic regions, which probably arise from a loss of balance in the geostrophic flow, unlike the ageostrophic flow elsewhere in the ocean, which probably arise directly from the wind forcing.

### 8.2 Stress Formulation

In addition to the mechanical coupling in eq. (16) (or eq. (3)), there is also thermal coupling between the ocean and atmosphere, which affects wind stress (Chelton et al., 2001, 2007; O'Neill et al., 2003). The air-sea thermal coupling changes the Marine Atmospheric Boundary Layer's stability and causes wind speed to change (Sweet et al., 1981; Businger & Shaw, 1984; R. d. Small et al., 2008). While the bulk stress formulation of (W. Large & Pond, 1981; W. G. Large et al., 1994) depends only on wind (relative) speed, the COARE bulk formulation (C. Fairall et al., 1997; C. W. Fairall et al., 2003) also accounts for the boundary layer stability due to the thermal air-sea coupling. This is beyond our scope here and we only use the W. Large and Pond (1981) bulk formulation of wind stress. It is also important to bear in mind that bulk parameterizations such as COARE and W. Large and Pond (1981) may become less accurate at sufficiently small length-scales and time-scales, although this is unlikely to be an issue in our study here.

### 8.3 Coarse-graining

Our analysis above (and in Rai et al. (2021)) has demonstrated that coarse-graining is an effective approach to disentangle eddy killing and highlighted its advantages over the traditional mean-eddy Reynolds decomposition. Yet, we wish to bring to the reader's attention some of the practical choices we have made in our coarse-graining analysis.

First, our choice of the graded Top-Hat kernel in eq. (11) to convolve with the fields is not unique. It is certainly possible to utilize one of the many other kernels such as Gaussian or Poisson functions. An in-depth discussion of the advantages of each is beyond our scope here (e.g., see Rivera et al. (2014)). We mention briefly that some of the desirable properties in our kernel is its positive semi-definiteness, which satisfies physical realizability conditions (Vreman et al., 1994). For example, it ensures density and energy remain positive (Buzzicotti, Aluie, et al., 2018), unlike other possibilities such as the Dirichlet kernel (Aluie & Eyink, 2009). Another advantage is that the Top-Hat function has a well-defined width, which can be easily associated with the length-scale at which we are decomposing the dynamics, unlike other kernels such as the Gaussian (Buzzicotti et al., 2021). Indeed, a convolution with $G_\ell$ in equation (11) is a spatial analogue to an $\ell$-day running time-average.

Second, when analyzing the flow close to continental boundaries or ice regions, we have to make a choice regarding the boundary treatment. For example, when coarse-graining the ocean velocity at location $\mathbf{x}$ near land, $\overline{\mathbf{u}}_\ell(\mathbf{x})$ is essentially a weighted average of the velocity within a region of radius $\ell/2$ around $\mathbf{x}$, which might include land. A practical choice we made in this work, as in Aluie et al. (2018), is to treat land as water with zero velocity over which the wind stress is also zero. This choice ensures that coarse-graining commutes with spatial derivatives (Buzzicotti et al., 2021), which is necessary for deriving the dynamics at

different scales self-consistently. Note that this is also consistent with numerical formulations of OGCMs, where land is often treated just like any ocean region but with an imposed zero velocity.

## 9 Summary and Discussion

Motivated by how to best mechanically couple winds to the ocean in models, this study builds on our previous work analyzing eddy killing (Rai et al., 2021), where we had used QuikSCAT winds and altimetry data to study wind work on the ocean surface as a function of length-scale. While it is well appreciated that stress formulated from absolute winds overestimates wind work (Duhaut & Straub, 2006), we show here that stress formulated from relative winds can introduce a significant bias in the opposite direction by underestimating wind work even when the atmosphere and ocean are coupled. By analyzing wind work as a function of length-scale, this study demonstrates how these biases from absolute and relative stress formulations are primarily at the mesoscales. We proposed a simple reformulation of the wind stress to correct such biases.

We were able to objectively disentangle wind work by these stress formulations at different length-scales using spatial coarse-graining. The approach is objective in the sense that it does not rely on preconceived notions of what constitutes a mesoscale eddy. We showed that coarse-graining can unravel mesoscale eddy-killing clearly, while the more traditional Reynolds averaging decomposition of the flow cannot.

We found that both absolute and relative wind stress formulations are reasonably accurate (within 10%) in how they force the large-scales, however, they differ starkly in their roles at the mesoscales. Absolute stress, $\boldsymbol{\tau}_a$, does negligible (albeit positive) work on the mesoscales with muted seasonality. On the other hand, relative stress, $\boldsymbol{\tau}_r$, yields eddy-killing (negative work) at the mesoscales. This eddy-killing by $\boldsymbol{\tau}_r$ is significantly exaggerated when the atmospheric resolution is coarser than the ocean's, which is the case in almost all general circulation model. The eddy-killing exaggeration bias persists at all times and is especially pronounced in dynamic regions like WBCs and ACC.

A main contribution was deriving a mathematical criterion (eq. (27)) for eddy killing to occur at any length-scale, which gives us insight into the physics of wind work as quantified by $EP^{Cg}$. This criterion provides the theoretical explanation for results in Rai et al. (2021) and shows that a mismatch in resolution between the atmosphere and ocean components of GCMs leads to an exaggeration in eddy-killing.

The analytical expression (eq. (26)) highlights the disproportionate effect small-scale winds $O(100)$ km can have on the dynamics of mesoscale ocean eddies, despite the dominant atmospheric motions being at length-scales larger than $O(10^3)$ km (e.g. Nastrom et al., 1984). The mechanical coupling between the atmosphere and the oceanic mesoscales can be significantly distorted if the atmospheric motions at those same scales are misrepresented in a model. We were able to infer that, on average, small-scale winds tend to be aligned with oceanic mesoscales at the surface, but are not sufficiently strong to energize them. The tendency for small-scale winds and currents to be aligned may be due to the so-called "re-energization" mechanism identified by Renault, Molemaker, McWilliams, et al. (2016), in which winds mechanically adjust to the ocean surface state. What we highlighted here, based on eq. (26), is that such atmospheric adjustment is not possible at the scale of oceanic eddies if the atmosphere's resolution is coarser than the ocean's even in coupled atmosphere-ocean models. Such resolution mismatch can lead to significant artifacts in the wind forcing of ocean mesoscales.

We proposed a simple recipe to correct for exaggerated eddy killing. The reformulated stress has no free parameters and relies on expressing stress using wind velocity relative to ocean surface currents at a coarsened resolution to match the atmosphere's. The reformulated stress $\boldsymbol{\tau}_{r2}$ showed remarkable improvement, which provided evidence that resolution

mismatch causes exaggerated eddy killing. We believe the simplicity of the recipe and its lack of any free parameters makes it especially appealing.

Our reformulated wind stress recipe may be thought of as an attempt to parameterise the unresolved alignment between the small-scale winds and ocean currents if the atmosphere has sufficient resolution. It is somewhat related, at least in spirit, to parameterizations of re-energization proposed by Renault et al. (2020) for ocean-only simulations. Adding a dynamic marine atmospheric boundary layer similar to the one suggested in Lemarié et al. (2017) that can resolve the feedbacks from the ocean could be another way to provide more correct forcing, albiet at a higher computation cost.

## Appendix A Wind Stress

A note on terminology that is common in geophysical fluid dynamics but may be confusing outside: the term "stress" used here refers to the *vector* $\boldsymbol{\tau}$ (N/m$^2$). This is physically related to the full stress *tensor* $\mathbf{T}$ via $\tau_i = T_{iz}$, as is commonly (and reasonably) assumed, since $\partial_z T_{iz}$ is the dominant force in the ocean surface momentum balance. Here, $\tau_i$ is the $i$-th horizontal component of the vector $\boldsymbol{\tau}$. Therefore, the power (in Watts) injected by the wind can be calculated from the inner product of geostrophic ocean velocity, $\mathbf{u}$, with the wind force (per unit volume) in the momentum equation, $\partial_z \boldsymbol{\tau}$, and integrating over volume:

$$\begin{aligned}
\text{wind work} &= \int dA \int_{-Ek}^{0} dz\ u_i \partial_z \tau_i \\
&= \int dA \int_{-Ek}^{0} dz\ \Big[\partial_z(u_i\tau_i) - \underbrace{(\partial_z u_i)\tau_i}_{=0}\Big] \\
&= \int dA\ \Big[u_i\tau_i|_{z=0} - \underbrace{u_i\tau_i}_{=0}|_{z=-Ek}\Big] \\
&= \int dA\ \mathbf{u}\cdot\boldsymbol{\tau}|_{z=0}
\end{aligned}$$

where $\partial_z \mathbf{u} = 0$ within the Ekman boundary layer ($< 100$ m) for the low-frequency flow at horizontal length-scales $> 50$ km, while $\boldsymbol{\tau} = 0$ below the Ekman boundary layer. The latter also explains the third expression above.

## Appendix B Regional Analysis

We generate masks for oceanic regions of interest shown in Fig. 5 over which we analyze eddy-killing. The equatorial mask is the $\pm 8°$ band, and the Southern Ocean mask is the $[35° - 65°\text{S}]$ band. The remaining masks are irregular and are intended to select strongly eddying regions with strong currents. Specifically, the masks satisfy $\frac{1}{2}|\langle \mathbf{u}_o \rangle|^2 + \frac{1}{2}\langle |\mathbf{u}'_o|^2 \rangle > 0.1$ m$^2$/s$^2$ in the Gulf Stream and Kuroshio, and $\frac{1}{2}|\langle \mathbf{u}_o \rangle|^2 + \frac{1}{2}\langle |\mathbf{u}'_o|^2 \rangle > 0.05$ m$^2$/s$^2$ in the remaining regions shown in Fig. 5. Subject to these thresholds, the masks lie within $[35° - 70°\text{S}]$ (ACC), $[15° - 85°\text{W}, 23° - 55°\text{N}]$ (Gulf Stream), $[120° - 180°\text{E}, 23° - 50°\text{N}]$ (Kuroshio), $[0° - 45°\text{E}, 15° - 40°\text{S}]$ (Agulhas), and $[40° - 75°\text{W}, 35° - 60°\text{S}]$ (Brazil-Malvinas).

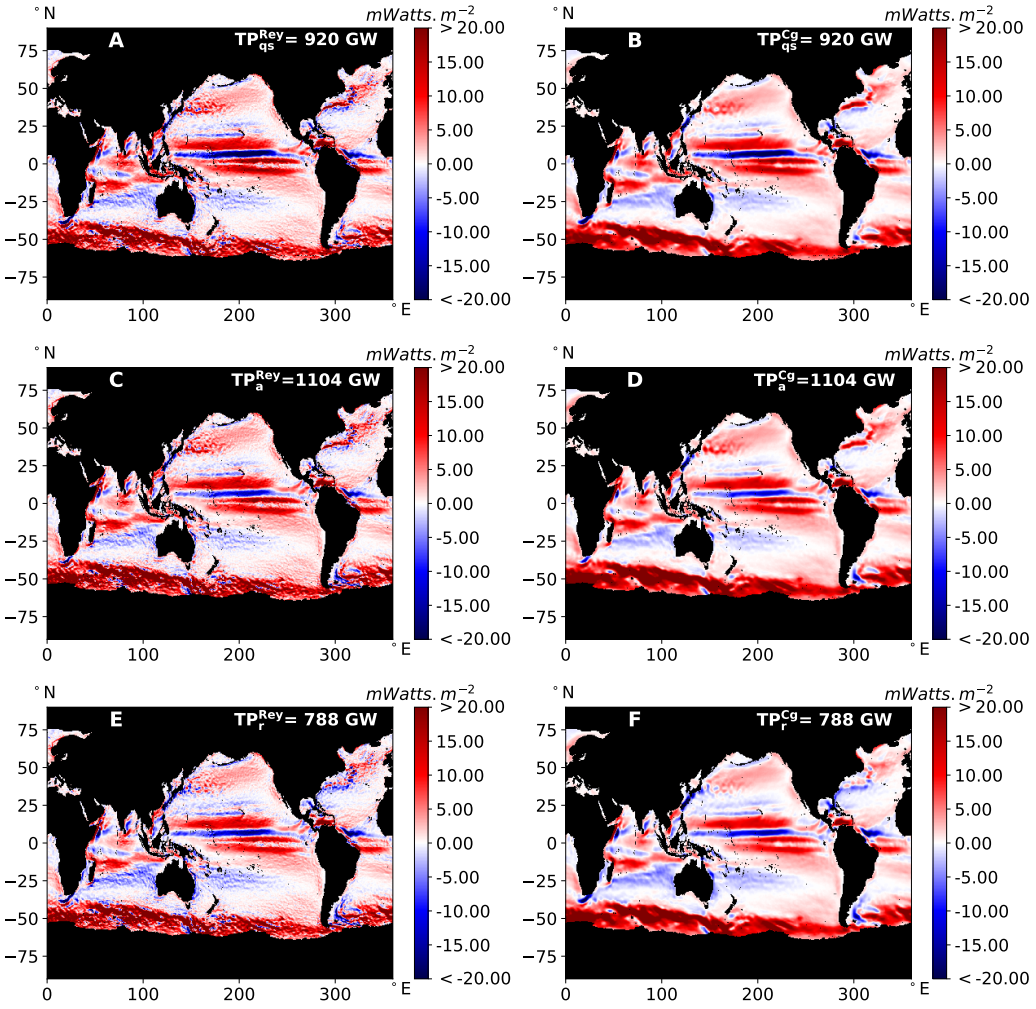


Figure A1: Total wind work (in W/m$^2$) to the ocean using Reynolds averaging (left column) and coarse-graining (right column). Different rows show the three stress formulations: QuikSCAT stress $\boldsymbol{\tau}_{qs}$ (top), NCEP absolute stress $\boldsymbol{\tau}_a$ (middle), NCEP relative stress $\boldsymbol{\tau}_r$ (bottom). Coarse-graining is performed with $\ell = 300$ km. All six panels are qualitatively similar and left panel have identical domain integrated value with right panel, except for subtle differences in the fine features. Note that areas in black include land and ocean regions with seasonal or permanent ice coverage.

## Data Availability Statement

All the data we have used are freely available for public access. The geostrophic currents data is available at CMEMS repository `https://doi.org/10.48670/moi-00148`. The QuikSCAT winds is available at The Physical Oceanography Distributed Active Archive Center (PO.DAAC) and be accessed from `https://podaac-opendap.jpl.nasa.gov/opendap/allData/quikscat/L3/jpl/v2/hdf/`. The 10m winds data from NCEP/DOE Reanalysis II is provided by the NOAA PSL, Boulder, Colorado, USA, from their website at `https://psl.noaa.gov/data/gridded/data.ncep.reanalysis2.html`


## Acknowledgments

SR and HA thank Benjamin Storer and Michele Buzzicotti for valuable discussions and suggestions. This research was funded by US NASA grant 80NSSC18K0772 and US NSF grant OCE-2123496. HA was also supported by US DOE grants DE-SC0020229, DE-SC0014318, and DE-SC0019329, US NSF grants PHY-2020249 and PHY-2206380, and US NNSA grants DE-NA0003856, DE-NA0003914, DE-NA0004134.

Computing time was provided by the National Energy Research Scientific Computing Center (NERSC) under Contract No. DE-AC02-05CH11231 and NASA's High-End Computing (HEC) Program through the NASA Center for Climate Simulation (NCCS) at Goddard Space Flight Center. This report was prepared as an account of work sponsored by an agency of the U.S. Government. Neither the U.S. Government nor any agency thereof, nor any of their employees, makes any warranty, express or implied, or assumes any legal liability or responsibility for the accuracy, completeness, or usefulness of any information, apparatus, product, or process disclosed, or represents that its use would not infringe privately owned rights. Reference herein to any specific commercial product, process, or service by trade name, trademark, manufacturer, or otherwise does not necessarily constitute or imply its endorsement, recommendation, or favoring by the U.S. Government or any agency thereof. The views and opinions of authors expressed herein do not necessarily state or reflect those of the U.S. Government or any agency thereof.

AVISO (https://www.aviso.altimetry.fr) Ssalto/Duacs altimeter products were produced and distributed by the Copernicus Marine and EnvironmentMonitoring Service (CMEMS) `https://resources.marine.copernicus.eu/?option=com_csw&task=results?option=com_csw&view=details&product_id=SEALEVEL_GLO_PHY_L4_REP_OBSERVATIONS_008_047`. NCEP winds were obtained from `https://www.esrl.noaa.gov/psd/` and the QuikSCAT Wind Vectors (JPL Version 2) data was obtained from `https://podaac-opendap.jpl.nasa.gov/opendap/allData/quikscat/L3/jpl/v2/hdf/`


## References


Alford, M. H. (2003). Improved global maps and 54-year history of wind-work on ocean inertial motions. *Geophysical Research Letters*, *30*(8).

Aluie, H. (2017, January). Coarse-grained incompressible magnetohydrodynamics: analyzing the turbulent cascades. *New Journal of Physics*, *19*, 025008.

Aluie, H. (2019). Convolutions on the sphere: commutation with differential operators. *GEM-International Journal on Geomathematics*, *10*(1), 9.

Aluie, H., & Eyink, G. L. (2009). Localness of energy cascade in hydrodynamic turbulence. II. Sharp spectral filter. *Physics of Fluids*, *21*(11), 115108.

Aluie, H., Hecht, M., & Vallis, G. K. (2018). Mapping the energy cascade in the north atlantic ocean: The coarse-graining approach. *Journal of Physical Oceanography*, *48*(2), 225–244.

Aluie, H., & Kurien, S. (2011, November). Joint downscale fluxes of energy and potential enstrophy in rotating stratified Boussinesq flows. *EPL (Europhysics Letters)*, *96*(4), 44006.

Bourassa, M. A., Legler, D. M., O'brien, J. J., & Smith, S. R. (2003). Seawinds validation with research vessels. *Journal of Geophysical Research: Oceans*, *108*(C2).

Burgess, B. H., Erler, A. R., & Shepherd, T. G. (2013). The troposphere-to-stratosphere transition in kinetic energy spectra and nonlinear spectral fluxes as seen in ecmwf analyses. *Journal of the atmospheric sciences*, *70*(2), 669–687.

Businger, J., & Shaw, W. (1984). The response of the marine boundary layer to mesoscale variations in sea-surface temperature. *Dynamics of atmospheres and oceans*, *8*(3-4), 267–281.

Buzzicotti, M., Aluie, H., Biferale, L., & Linkmann, M. (2018, March). Energy transfer in turbulence under rotation. *Physical Review Fluids*, *3*(3), 291.

Buzzicotti, M., Linkmann, M., Aluie, H., Biferale, L., Brasseur, J., & Meneveau, C. (2018). Effect of filter type on the statistics of energy transfer between resolved and subfilter scales from a-priori analysis of direct numerical simulations of isotropic turbulence. *Journal of Turbulence*, *19*(2), 167–197.

Buzzicotti, M., Storer, B. A., Griffies, S. M., & Aluie, H. (2021). A coarse-grained decomposition of surface geostrophic kinetic energy in the global ocean. *Earth and Space Science Open Archive*, 58. Retrieved from `https://doi.org/10.1002/essoar.10507290.1` doi: 10.1002/essoar.10507290.1

Bye, J. (1985). Large-scale momentum exchange in the coupled atmosphere-ocean. *Elsevier oceanography series*, *40*, 51–61.

Chelton, D. B., Esbensen, S. K., Schlax, M. G., Thum, N., Freilich, M. H., Wentz, F. J., ... Schopf, P. S. (2001). Observations of coupling between surface wind stress and sea surface temperature in the eastern tropical pacific. *Journal of Climate*, *14*(7), 1479–1498.

Chelton, D. B., & Freilich, M. H. (2005). Scatterometer-Based Assessment of 10-m Wind Analyses from the Operational ECMWF and NCEP Numerical Weather Prediction Models. *Monthly Weather Review*, *133*, 409–429.

Chelton, D. B., Schlax, M. G., Freilich, M. H., & Milliff, R. F. (2004). Satellite measurements reveal persistent small-scale features in ocean winds. *science*, *303*(5660), 978–983.

Chelton, D. B., Schlax, M. G., & Samelson, R. M. (2007). Summertime coupling between sea surface temperature and wind stress in the california current system. *Journal of Physical Oceanography*, *37*(3), 495–517.

Cornillon, P., & Park, K. (2001). Warm core ring velocities inferred from nscat. *Geophysical research letters*, *28*(4), 575–578.

Dawe, J. T., & Thompson, L. (2006). Effect of ocean surface currents on wind stress, heat flux, and wind power input to the ocean. *Geophysical Research Letters*, *33*(9).

Desbiolles, F., Bentamy, A., Blanke, B., Roy, C., Mestas-Nuñez, A. M., Grodsky, S. A., ... Maes, C. (2017). Two decades [1992–2012] of surface wind analyses based on satellite scatterometer observations. *Journal of Marine Systems*, *168*, 38–56.

Dewar, W. K., & Flierl, G. R. (1987). Some effects of the wind on rings. *Journal of physical oceanography*, *17*(10), 1653–1667.

Dufour, C. O., Griffies, S. M., de Souza, G. F., Frenger, I., Morrison, A. K., Palter, J. B., ... others (2015). Role of mesoscale eddies in cross-frontal transport of heat and biogeochemical tracers in the southern ocean. *Journal of Physical Oceanography*, *45*(12), 3057–3081.

Duhaut, T. H., & Straub, D. N. (2006). Wind stress dependence on ocean surface velocity: Implications for mechanical energy input to ocean circulation. *Journal of physical oceanography*, *36*(2), 202–211.

Eden, C., & Dietze, H. (2009). Effects of mesoscale eddy/wind interactions on biological new production and eddy kinetic energy. *Journal of Geophysical Research: Oceans*, *114*(C5).

Eyink, G. L. (2005, July). Locality of turbulent cascades. *Physica D: Nonlinear Phenomena*, *207*(1-2), 91–116.

Fairall, C., White, A., Edson, J., & Hare, J. (1997). Integrated shipboard measurements of the marine boundary layer. *Journal of Atmospheric and Oceanic Technology*, *14*(3),

338–359.

Fairall, C. W., Bradley, E. F., Hare, J., Grachev, A. A., & Edson, J. B. (2003). Bulk parameterization of air–sea fluxes: Updates and verification for the coare algorithm. *Journal of climate*, *16*(4), 571–591.

Fangohr, S., & Kent, E. C. (2012, May). An Estimate of Structural Uncertainty in QuikSCAT Wind Vector Retrievals. *Journal of Applied Meteorology and Climatology*, *51*(5), 954–961.

Ferrari, R., & Wunsch, C. (2009). Ocean circulation kinetic energy: Reservoirs, sources, and sinks. *Annual Review of Fluid Mechanics*, *41*, 253–282.

Flexas, M. M., Thompson, A. F., Torres, H. S., Klein, P., Farrar, J. T., Zhang, H., & Menemenlis, D. (2019). Global estimates of the energy transfer from the wind to the ocean, with emphasis on near-inertial oscillations. *Journal of geophysical research. Oceans*, *124*(8), 5723.

Fu, L.-L., & Chao, Y. (1997). The sensitivity of a global ocean model to wind forcing: A test using sea level and wind observations from satellites and operational wind analysis. *Geophysical research letters*, *24*(14), 1783–1786.

Garçon, V. C., Oschlies, A., Doney, S. C., McGillicuddy, D., & Waniek, J. (2001). The role of mesoscale variability on plankton dynamics in the north atlantic. *Deep Sea Research Part II: Topical Studies in Oceanography*, *48*(10), 2199–2226.

Geernaert, G., & Katsaros, K. B. (1986). Incorporation of stratification effects on the oceanic roughness length in the derivation of the neutral drag coefficient. *Journal of physical oceanography*, *16*(9), 1580–1584.

Germano, M. (1992). Turbulence: the filtering approach. *Journal of Fluid Mechanics*, *238*, 325–336.

Hausmann, U., & Czaja, A. (2012). The observed signature of mesoscale eddies in sea surface temperature and the associated heat transport. *Deep Sea Research Part I: Oceanographic Research Papers*, *70*, 60–72.

Held, I., Guo, H., Adcroft, A., Dunne, J., Horowitz, L., Krasting, J., ... others (2019). Structure and performance of gfdl's cm4. 0 climate model. *Journal of Advances in Modeling Earth Systems*, *11*(11), 3691–3727. doi: 10.1029/2019MS001829.

Hughes, C. W., & Wilson, C. (2008). Wind work on the geostrophic ocean circulation: An observational study of the effect of small scales in the wind stress. *Journal of Geophysical Research: Oceans*, *113*(C2).

Hutchinson, D. K., Hogg, A. M. C., & Blundell, J. R. (2010). Southern ocean response to relative velocity wind stress forcing. *Journal of Physical Oceanography*, *40*(2), 326–339.

Kang, D., & Curchitser, E. N. (2015, April). Energetics of Eddy–Mean Flow Interactions in the Gulf Stream Region. *Journal of Physical Oceanography*, *45*(4), 1103–1120.

Kelly, K. A., Dickinson, S., McPhaden, M. J., & Johnson, G. C. (2001). Ocean currents evident in satellite wind data. *Geophysical Research Letters*, *28*(12), 2469–2472.

Khani, S., Jansen, M. F., & Adcroft, A. (2019). Diagnosing subgrid mesoscale eddy fluxes with and without topography. *Journal of Advances in Modeling Earth Systems*, *11*(12), 3995–4015.

Kundu, P. K., Cohen, I. M., & Dowling, D. R. (2015). *Fluid mechanics*. Academic press.

Lagerloef, G. S., Mitchum, G. T., Lukas, R. B., & Niiler, P. P. (1999). Tropical pacific near-surface currents estimated from altimeter, wind, and drifter data. *Journal of Geophysical Research: Oceans*, *104*(C10), 23313–23326.

Large, W., & Pond, S. (1981). Open ocean momentum flux measurements in moderate to strong winds. *Journal of physical oceanography*, *11*(3), 324–336.

Large, W. G., McWilliams, J. C., & Doney, S. C. (1994). Oceanic vertical mixing: A review and a model with a nonlocal boundary layer parameterization. *Reviews of Geophysics*, *32*(4), 363–403.

Lemarié, F., Samson, G., Redelsperger, J.-L., Giordani, H., Brivoal, T., & Madec, G. (2021). A simplified atmospheric boundary layer model for an improved representation of air–sea interactions in eddying oceanic models: implementation and first evaluation in

nemo (4.0). *Geoscientific Model Development*, *14*(1), 543–572.

Lemarié, F., Samson, G., Redelsperger, J.-L., Giordani, H., & Madec, G. (2017). Toward an improved representation of air-sea interactions in high-resolution global ocean forecasting systems..

Liu, Y., Yu, L., & Chen, G. (2020). Characterization of sea surface temperature and air-sea heat flux anomalies associated with mesoscale eddies in the south china sea. *Journal of Geophysical Research: Oceans*, *125*(4), e2019JC015470.

Mazloff, M. R., Gille, S. T., & Cornuelle, B. (2014, December). Improving the geoid: Combining altimetry and mean dynamic topography in the California coastal ocean. *Geophysical Research Letters*, *41*(24), 8944–8952.

Mémery, L., Reverdin, G., Paillet, J., & Oschlies, A. (2005). Introduction to the pomme special section: Thermocline ventilation and biogeochemical tracer distribution in the northeast atlantic ocean and impact of mesoscale dynamics. *Journal of Geophysical Research: Oceans*, *110*(C7).

Menemenlis, D., Hill, C., Henze, C. E., Wang, J., & Fenty, I. (n.d.). *Southern ocean pre-swot level-4 hourly mitgcm llc4320 native grid 2km oceanographic dataset.* doi: 10.5067/PRESW-ASJ10

Munk, W., & Wunsch, C. (1998). Abyssal recipes ii: Energetics of tidal and wind mixing. *Deep Sea Research Part I: Oceanographic Research Papers*, *45*(12), 1977–2010.

Nastrom, G., Gage, K., & Jasperson, W. (1984). Kinetic energy spectrum of large-and mesoscale atmospheric processes. *Nature*, *310*(5972), 36–38.

O'Neill, L. W., Chelton, D. B., & Esbensen, S. K. (2003). Observations of sst-induced perturbations of the wind stress field over the southern ocean on seasonal timescales. *Journal of Climate*, *16*(14), 2340–2354.

O'Neill, L. W. (2012). Wind speed and stability effects on coupling between surface wind stress and sst observed from buoys and satellite. *Journal of Climate*, *25*(5), 1544–1569.

Pacanowski, R. (1987). Effect of equatorial currents on surface stress. *Journal of physical oceanography*, *17*(6), 833–838.

Pei, Q., Sheng, J., & Ohashi, K. (2022). Numerical study of effects of winds and tides on monthly-mean circulation and hydrography over the southwestern scotian shelf. *Journal of Marine Science and Engineering*, *10*(11), 1706.

Quilfen, Y., Chapron, B., Elfouhaily, T., Katsaros, K., & Tournadre, J. (1998, April). Observation of tropical cyclones by high resolution scatterometry. *Journal of Geophysical Research-Oceans*, *103*(C), 7767–7786.

Rai, S., Hecht, M., Maltrud, M., & Aluie, H. (2021). Scale of oceanic eddy killing by wind from global satellite observations. *Science Advances*, *7*(28), eabf4920.

Renault, L., Marchesiello, P., Masson, S., & Mcwilliams, J. C. (2019). Remarkable control of western boundary currents by eddy killing, a mechanical air-sea coupling process. *Geophysical Research Letters*, *46*(5), 2743–2751.

Renault, L., Masson, S., Arsouze, T., Madec, G., & Mcwilliams, J. C. (2020, February). Recipes for How to Force Oceanic Model Dynamics. *Journal of Advances in Modeling Earth Systems*, *12*(2), 51.

Renault, L., McWilliams, J. C., & Gula, J. (2018). Dampening of submesoscale currents by air-sea stress coupling in the californian upwelling system. *Scientific reports*, *8*(1), 1–8.

Renault, L., McWilliams, J. C., & Masson, S. (2017). Satellite observations of imprint of oceanic current on wind stress by air-sea coupling. *Scientific reports*, *7*(1), 17747.

Renault, L., Molemaker, M. J., Gula, J., Masson, S., & McWilliams, J. C. (2016). Control and stabilization of the gulf stream by oceanic current interaction with the atmosphere. *Journal of Physical Oceanography*, *46*(11), 3439–3453.

Renault, L., Molemaker, M. J., McWilliams, J. C., Shchepetkin, A. F., Lemarié, F., Chelton, D., ... Hall, A. (2016). Modulation of wind work by oceanic current interaction with the atmosphere. *Journal of Physical Oceanography*, *46*(6), 1685–1704.

Rivera, M. K., Aluie, H., & Ecke, R. E. (2014, May). The direct enstrophy cascade of two-dimensional soap film flows. *Physics of Fluids*, *26*(5).

Roberts, M. (2017). *Mohc hadgem3-gc31-lm model output prepared for cmip6 highresmip.* Earth System Grid Federation. Retrieved from `https://doi.org/10.22033/ESGF/CMIP6.1321` doi: 10.22033/ESGF/CMIP6.1321

Roberts, M. (2018). *Mohc hadgem3-gc31-hh model output prepared for cmip6 highresmip.* Earth System Grid Federation. Retrieved from `https://doi.org/10.22033/ESGF/CMIP6.445` doi: 10.22033/ESGF/CMIP6.445

Ryzhov, E., Kondrashov, D., Agarwal, N., & Berloff, P. (2019). On data-driven augmentation of low-resolution ocean model dynamics. *Ocean Modelling*, *142*, 101464.

Sadek, M., & Aluie, H. (2018, December). Extracting the spectrum of a flow by spatial filtering. *Physical Review Fluids*, *3*(12), 124610.

Scott, R. B., & Xu, Y. (2009). An update on the wind power input to the surface geostrophic flow of the world ocean. *Deep Sea Research Part I: Oceanographic Research Papers*, *56*(3), 295–304.

Semmler, T., Danilov, S., Rackow, T., Sidorenko, D., Hegewald, J., Sein, D., ... Jung, T. (2017). *Awi awi-cm 1.1 hr model output prepared for cmip6 highresmip.* Earth System Grid Federation. Retrieved from `https://doi.org/10.22033/ESGF/CMIP6.1202` doi: 10.22033/ESGF/CMIP6.1202

Seo, H., Miller, A. J., & Norris, J. R. (2016). Eddy–wind interaction in the california current system: Dynamics and impacts. *Journal of Physical Oceanography*, *46*(2), 439–459.

Small, R. d., deSzoeke, S. P., Xie, S., O'neill, L., Seo, H., Song, Q., ... Minobe, S. (2008). Air–sea interaction over ocean fronts and eddies. *Dynamics of Atmospheres and Oceans*, *45*(3-4), 274–319.

Small, R. J., Bacmeister, J., Bailey, D., Baker, A., Bishop, S., Bryan, F., ... others (2014). A new synoptic scale resolving global climate simulation using the community earth system model. *Journal of Advances in Modeling Earth Systems*, *6*(4), 1065–1094.

Srinivasan, K., Mcwilliams, J. C., Molemaker, M. J., & Barkan, R. (2019, July). Submesoscale Vortical Wakes in the Lee of Topography. *Journal of Physical Oceanography*, *49*, 1949–1971.

Stammer, D. (1997, August). Global characteristics of ocean variability estimated from regional TOPEX/POSEIDON altimeter measurements. *Journal of Physical Oceanography*, *27*(8), 1743–1769.

Stammer, D., & Cazenave, A. (Eds.). (2017). *Satellite altimetry over oceans and land surfaces* (1st ed.). Boca Raton: CRC Press.

Stoffelen, A., & Anderson, D. (1997). Scatterometer data interpretation: Measurement space and inversion. *Journal of atmospheric and oceanic technology*, *14*(6), 1298–1313.

Storer, B. A., Buzzicotti, M., Khatri, H., Griffies, S. M., & Aluie, H. (2022). Global energy spectrum of the general oceanic circulation. *arXiv preprint arXiv:2208.04859*. doi: 10.48550/arXiv.2208.04859

Sui, Y., Sheng, J., Tang, D., & Xing, J. (2022). Study of storm-induced changes in circulation and temperature over the northern south china sea during typhoon linfa. *Continental Shelf Research*, *249*, 104866.

Swart, N. C., Cole, J. N., Kharin, V. V., Lazare, M., Scinocca, J. F., Gillett, N. P., ... Sigmond, M. (2019). *Cccma canesm5-canoe model output prepared for cmip6 scenariomip ssp585.* Earth System Grid Federation. Retrieved from `https://doi.org/10.22033/ESGF/CMIP6.10276` doi: 10.22033/ESGF/CMIP6.10276

Sweet, W., Fett, R., Kerling, J., & La Violette, P. (1981). Air-sea interaction effects in the lower troposphere across the north wall of the gulf stream. *Monthly Weather Review*, *109*(5), 1042–1052.

Tokinaga, H., Tanimoto, Y., & Xie, S.-P. (2005). Sst-induced surface wind variations over the brazil–malvinas confluence: Satellite and in situ observations. *Journal of climate*, *18*(17), 3470–3482.

Vallis, G. K. (2017). *Atmospheric and oceanic fluid dynamics.* Cambridge University Press.

Von Storch, J.-S., Sasaki, H., & Marotzke, J. (2007). Wind-generated power input to the

deep ocean: An estimate using a 1/10 general circulation model. *Journal of physical oceanography*, *37*(3), 657–672.

Vreman, B., Geurts, B., & Kuerten, H. (1994). Realizability conditions for the turbulent stress tensor in large-eddy simulation. *Journal of Fluid Mechanics*, *278*, 351–362.

Wang, W., & Huang, R. X. (2004a). Wind Energy Input to the Ekman Layer. *Journal of Physical Oceanography*, *34*, 1267–.

Wang, W., & Huang, R. X. (2004b). Wind Energy Input to the Surface Waves. *Journal of Physical Oceanography*, *34*, 1276–.

Watanabe, M., & Hibiya, T. (2002). Global estimates of the wind-induced energy flux to inertial motions in the surface mixed layer. *Geophysical Research Letters*, *29*(8).

Weissman, D. E., Davidson, K. L., Brown, R. A., Friehe, C. A., & Li, F. (1994). The Relationship Between the Microwave Radar Cross-Section and Both Wind-Speed and Stress - Model Function Studies Using Frontal Air-Sea Interaction Experiment Data. *Journal of Geophysical Research*, *99*(C5), 10087–10108.

Wunsch, C. (1998). The work done by the wind on the oceanic general circulation. *Journal of Physical Oceanography*, *28*(11), 2332–2340.

Wunsch, C., Ferrari, R., et al. (2004). Vertical mixing, energy, and the general circulation of the oceans. *Annual Review of Fluid Mechanics*, *36*(1), 281–314.

Xu, C., Zhai, X., & Shang, X.-D. (2016). Work done by atmospheric winds on mesoscale ocean eddies. *Geophysical Research Letters*, *43*(23).

Xu, Y., & Scott, R. B. (2008). Subtleties in forcing eddy resolving ocean models with satellite wind data. *Ocean Modelling*, *20*(3), 240–251.

Yan, X., Kang, D., Curchitser, E. N., & Pang, C. (2019, March). Energetics of Eddy-Mean Flow Interactions along the Western Boundary Currents in the North Pacific. *Journal of Physical Oceanography*, *49*, 789–810.

Yu, L., & Jin, X. (2014, August). Insights on the OAFlux ocean surface vector wind analysis merged from scatterometers and passive microwave radiometers (1987 onward). *Journal of Geophysical Research-Oceans*, *119*(8), 5244–5269.

Zhai, X., & Greatbatch, R. J. (2007). Wind work in a model of the northwest atlantic ocean. *Geophysical research letters*, *34*(4).